Consistent and Contrasting Aspects of the Geomagnetic Field Across Epochs With Distinct Reversal Frequencies Revealed by Modeling the Kiaman Superchron

Daniele Brandt[1] , **Marcia Ernesto[1]** , and **Catherine Constable[2]**

[1]Departamento de Geofísica, Instituto de Astronomia, Geofísica e Ciências Atmosféricas, Universidade de São Paulo, São Paulo, Brazil, [2]Institute of Geophysics and Planetary Physics, Scripps Institution of Oceanography, University of California at San Diego, La Jolla, CA, USA

Abstract This work presents an extensive directional paleomagnetic database of the Kiaman reversed superchron. It is composed of 1,459 paleomagnetic directions from igneous rocks corresponding to 91 data sets (or paleomagnetic poles). An almost constant behavior of more concentrated and circular distributions for latitudes higher than 10° was found, which contrasts strongly with predictions of the representative models for the past few million years. We searched for simplified and spatially covariant Giant Gaussian Process (GGP) models that best explain the directional distribution of the Kiaman database. We used the mean strength based on the mean of virtual dipole moment (VDM) results for the period drawn from the available databases. Among the tested models, the one that best explains the directional paleosecular variation of the Kiaman database is the covariant type. According to this model, the correlations between the Gaussian coefficients are valid for the last 10 Myr and the Kiaman superchron. The resulting GGP models have β parameters similar to the 0–10 Ma models, which indicates that the relation between symmetric and antisymmetric families appears unchanged in the geological past. The relative variability of the Kiaman field, as inferred from the ratio $\alpha/\overline{g_1^0}$ from GGP models, is lower than for the past 10 Myr. Thus, as well as the paleointensity, $\alpha/\overline{g_1^0}$ seems to be a proxy that can be used for evaluating the geomagnetic development along the geological time.

1. Introduction

The study of the geomagnetic field on a geological timescale brings imperative links to investigating the ancient deep Earth, particularly in understanding of the behavior of the field with regard to the polarity changes. Throughout the Earth's history, the field polarity has changed continuously, intercalating periods of relatively high-frequency polarity changes and others with practically no changes. Long time intervals comprising tens of million years of a single polarity define the superchrons. Three superchrons have been recognized in the Phanerozoic: the Moyero Superchron of reversed polarity during the Ordovician (Pavlov et al., 2012), the Permo-Carboniferous Reversed Superchron (~267–318 Ma; Hounslow & Balabarov, 2016; Opdyke & Channell, 1996), also known as the Kiaman Superchron, and the Cretaceous Normal Superchron (CNS: 84–126 Ma, Ogg, 2012a, 2012b). The origin of the superchrons is not yet well understood. Some authors attribute it to deep mantle plume activity (Larson & Olson, 1991). The collapse of the superplumes causes a decrease in the heat flux in the core-mantle boundary. It also affects the lateral heterogeneity of that interface, triggering a superchron (Amit & Olson, 2015). The regrowth of a plume could again allow the occurrence of field reversals.

Recently, several papers have focused on the field behavior during the superchrons (e.g., de Oliveira et al., 2018; Doubrovine et al., 2019). The main scope is to verify if the long-term variations of the Earth's magnetic field (the paleosecular variation, PSV) differ from the behavior during high activity times.

Models of PSV are statistical models based on the premise that the Earth's magnetic field varies around a mean configuration and the paleomagnetic records are spot random readings of it. The fundamental hypothesis of paleomagnetism, that the average field is well described by a geocentric axial dipole (GAD) field, is normally considered reasonable for times older than the last few million years. Changing overall characteristics of the field through geological time may be assessed by parameters such as reversal frequency (e.g., Driscoll & Evans, 2016; Hounslow, 2016), the strength of the mean-field (e.g., Kulakov et al., 2019; Shcher-

bakov & Sycheva, 2013; Tarduno et al., 2006), latitudinal dependence of the virtual geomagnetic pole (VGP) scatter (e.g., Biggin, Strik, & Langereis, 2008; Biggin, van Hinsbergen, Langereis, Straathof, & Deenen, 2008; McFadden et al., 1991; Smirnov et al., 2011), and the shape and scale of the directional distributions (Tauxe & Kodama, 2009).

The latitudinal dependence of the VGPs scatter S_F, associated with the geomagnetic field variations, is defined by the a and b shape parameters in Model G (McFadden et al., 1988) in the form:

$$S_F = \sqrt{a^2 + b^2\lambda^2}, \tag{1}$$

where a^2 and $b^2\lambda^2$ are, respectively, the VGP scatter caused by the symmetric (even) and the antisymmetric (odd) families of the geomagnetic field described by spherical harmonic functions.

PSV models based on giant Gaussian processes (GGPs) can be used to predict the distribution of directions at any point of the Earth (e.g., BB18, Bono et al., 2020; BCE19, Brandt et al., 2020; CJ98, Constable & Johnson, 1999; CP88, Constable & Parker, 1988; QC96, Quidelleur & Courtillot, 1996; TK03, Tauxe & Kent, 2004). The TK03 model is the most simplified version of the GGP models, as it has a mean GAD with an intensity of $\overline{g_1^0} = -18\,\mu\text{T}$ and only two parameters, α, and β, define the whole collection of standard deviations of spherical harmonic Gauss coefficients for every degree l and order m as shown in Equations 2 and 3.

$$\left(\sigma_l^m\right)^2 = \frac{\left(R_C/R_E\right)^{2l}\alpha^2}{(l+1)(2l+1)} \text{ for } l-m = even, \tag{2}$$

$$\left(\sigma_l^m\right)^2 = \frac{\left(R_C/R_E\right)^{2l}\alpha^2\beta^2}{(l+1)(2l+1)} \text{ for } l-m = odd \tag{3}$$

where R_C / R_E is the core-Earth radius ratio (0.547), and α and β are fitted parameters.

Using these relations and assuming the same intensity as TK03 for $\overline{g_1^0}$, Brandt et al. (2020) proposed a new simplified GGP model (BCE19). This model was fitted to an up-to-date directional paleomagnetic database from lavas of the last 10 My (PSV10; Cromwell et al., 2018), using the shape and scale of directional distributions (Brandt et al., 2020). Bono et al. (2020) built a new family of GGP models (BB18 and BB18.Z3), that follow the simplified idea of TK03 model (Equations 2 and 3) but defining σ_1^0 independently and inserting correlations between some pairs of Gaussian coefficients, which are $\left(g_1^0,g_3^0\right)$, $\left(g_1^1,g_3^1\right)\left(h_1^1,h_3^1\right)$, $\left(g_2^0,g_4^0\right)$, $\left(g_2^1,g_4^1\right)$, $\left(h_2^1,h_4^1\right)$, $\left(g_2^2,g_4^2\right)$, and $\left(h_2^2,h_4^2\right)$. This modification changed the simplified GGP models into a new type of PSV models, the Covariant GGP Models, which improve the fit to the latitudinal variation of the dispersion of the VGPs and the paleointensity results from the last 10 Ma (PSV10 database).

Since the first application of Model G to the geological past (McFadden et al., 1991) the superchrons have shown a more prominent latitudinal variation of VGP dispersion (S_F), and a reduced equatorial VGP scatter compared to periods of higher reversal frequency. Other analyses for the Phanerozoic superchrons using Model G (Biggin, van Hinsbergen, et al., 2008; de Oliveira et al., 2018; Doubrovine et al., 2019) also showed low equatorial and strong latitudinal dependence of S_F, with high ratio b/a (where b and a are the shape parameters of Model G, Equation 1). However, recent compilations also demonstrate strong latitudinal dependence of S_F and a high ratio b/a, for the past 10 Ma, when the field was reversing more frequently (Cromwell et al., 2018). Because of that, the ratio b/a is not a reliable proxy for reversal frequency (Doubrovine et al., 2019). Recent results indicate that the most reliable parameters for revealing significant changes in the geomagnetic field behavior are the shape parameter a from Model G and the moment of the mean dipole in the geological past (Kulakov et al., 2019; Sprain et al., 2020).

The GGP models were developed to describe the PSV behavior of the last few million years. Few tests have been performed to check whether those models are suitable to describe the more ancient geomagnetic field (Tauxe & Kodama, 2009; Tauxe et al., 2008). However, the TK03 model has been used as a reference when

the elongation/inclination (*E/I*) method is applied to sedimentary rocks, even for ages where the validity of TK03 has not been tested. This includes rocks with ages assigned to the Kiaman superchron (e.g., Brandt et al., 2009; Franco et al., 2012, Haldan et al., 2009). If the distribution of directions of a superchron is less or more scattered than the recent field but maintains the shape of the distribution with the same elongation for a given inclination, then the use of the TK03 model as a reference guide for superchrons is not incorrect, and the *E/I* method can be used. Available paleomagnetic data sets of Kiaman igneous rocks spanning the longest times exhibit smaller elongations than in the TK03 model. However, the high uncertainties make the results inconclusive (Bazhenov et al., 2016; Haldan et al., 2014). Brandt et al. (2019) made another attempt using sedimentary records and observed that the recent-field TK03 model is incompatible with the VGP scatter of the three Kiaman data sets they analyzed. But due to the scarcity of paleomagnetic series long enough to properly evaluate the elongation of the directional distributions for the Kiaman, this issue remains still open. It is still unknown whether the TK03 or the new GGP models BCE19 and BB18 are valid for the Kiaman times.

In summary, GGP models for times older than 10 Ma are still not established. This new work will focus on the directional distribution of the Kiaman paleomagnetic field, creating a new comprehensive igneous database (the paleomagnetic database of Kiaman Reversed Superchron [PDKRS]). Directional analyses are made following the strategies used by Brandt et al. (2020), followed by discussions on which GGP model best describes the Kiaman superchron and the similarities and disparities compared to GGP models for the recent field.

2. Methods

We focused on the field directional behavior to describe the PSV of the Kiaman geomagnetic field. A paleomagnetic database with data grouped in paleolatitude bands was constructed. The VGP scatter along with the shape and scale analyses of directional PSV was evaluated. New PSV models were fit to the resulting parameters.

2.1. Data Compilation and Selection

The Global Paleomagnetic Database (McElhinny & Lock, 1996) was the main source of paleomagnetic data collected for the Kiaman interval. It contains abundant information about the paleomagnetic poles organized in an easily searchable table. More than 70% of the references compiled in this work came from that database; the remainder 30% came from the Magic Database, and PINT database, and from bibliographic searching.

The initial criteria used for selecting the directional data sets were:

1. Paleomagnetic poles from igneous rocks only.
2. Primary magnetization with the same age as the studied rock.
3. Age of the paleomagnetic pole and rock unit compatible with the Kiaman interval (267–318 Ma).
4. All samples were demagnetized with demagnetization code DC $\geq$ 2 (McElhinny & Lock, 1996).

As a second step, tables containing declination and inclination from each site contributing to the pole were prepared using data taken from the original publication. More information about the reliability of the data, the rock type of each site, and statistical parameters were also computed. Additional filtering criteria were then applied:

5. Exclusion of sedimentary sites (there are some studies with a different type of rocks included), to avoid inclination shallowing effects or temporal smoothing during remanence acquisition.
6. Exclusion of unreliable sites as indicated by the authors.
7. Only data sets with at least five independent sites were considered for adequate temporal sampling.
8. Further evaluation of whether the data set distribution sampled the geomagnetic PSV adequately was based on the N-dependent A_{95} envelope (Deenen et al., 2011), as given by the upper and lower limits of the 95% confidence angle of paleomagnetic poles.

The A_{95} envelope procedure in item 8 supposes that a data set with an A_{95} higher than the maximum limit contains a significant additional contribution to the VGP dispersion apart from PSV and is, therefore, "unreliable"; an A_{95} below the lower limit is probably under-representing the PSV. Deenen et al. (2011) originally proposed limits determined from VGP scatter observed throughout Earth's history. As the PSV during a superchron has been related to a reduction in VGP scatter (Biggin, van Hinsbergen, et al., 2008; Brandt et al., 2019; Doubrovine et al., 2019; Franco et al., 2012; Haldan et al., 2009; Haldan et al., 2014; Oliveira et al., 2018) the lower limit of A_{95} given by Deenen et al. (2011) may be unrealistic for the PDKRS. Therefore, limits of maximum and minimum A_{95} were re-evaluated for this study based on the newly compiled data set.

To find the proper A_{95} limits to use in this work, we first rotated each data set so that the mean VGP corresponds to the geographic pole. After that, we merged the data from the Northern and Southern Hemispheres using paleolatitude bands of 10° width. The highest and lowest values of the estimate dispersion, K_{min}, and K_{max} (Fisher, 1953) for bands with more than 50 VGPs were used to define a new A_{95} envelope, according to the method described by Deenen et al. (2011). We considered the use of this approach for removal of the data sets that have discrepant signatures when compared to the overall behavior of the entire database. We recommend its use only with PDKRS. For other periods we recommend the limits presented by Deenen et al. (2011) related to a more comprehensive period of geological ages.

2.2. VGP Scatter and Model G-Type PSV Analysis

The VGP scatter, S_F, associated with the PSV of the field was calculated as follows:

$$S_F = \sqrt{S^2 - \frac{S_w^2}{\overline{n}}} \tag{4}$$

$$S = \sqrt{\frac{\sum \Delta_i^2}{N-1}} \tag{5}$$

$$\frac{S_w^2}{\overline{n}} = 0.335 \overline{\alpha_{95}}^2 \frac{2\left(1 + 3sin^2\lambda\right)^2}{\left(5 + 3sin^2\lambda\right)} \tag{6}$$

where S is the overall dispersion of VGPs and $\frac{S_w^2}{\overline{n}}$ is the correction associated with the intrasite dispersion S_w (McElhinny & McFadden, 1997); Δ_i is the angular difference between each VGP and the paleomagnetic pole; N is the number of sites; $\overline{n}$ is the mean number of specimens and $\overline{\alpha_{95}}$ is the mean α_{95} of the sites in the data set. For data sets without α_{95} information, a mean value from the whole database was used (average of 8.2°). The cutoff angle for calculating the mean paleomagnetic pole was defined using Vandamme's (1994) iterative process. The determination of paleolatitudes is explained below (Section 2.3). The 95% confidence limits of S_F were determined using 1,000 bootstrapped samples. The shape parameters a and b (Equation 1) of Model G (McFadden et al., 1988), for S_F vs. paleolatitude λ results, were found using the function *"optimize.leastsq"* from the *"Scipy"* Python library for least squares optimization in nonlinear problems. Confidence limits for a and b were found using the lower and upper limits of S_F values (in the same way as Biggin, Strik, et al., 2008; Oliveira et al., 2018).

2.3. Merging Data Sets

The size of the Permo-Carboniferous paleomagnetic records from individual studies is not usually large enough to guarantee adequate sampling of PSV. We grouped the directional data according to their paleolatitudes, thus enlarging the data sets. This procedure helped to improve the directional PSV determinations, as is commonly required for the PSV studies (e.g., Constable & Parker, 1988; Tauxe & Kent, 2004).
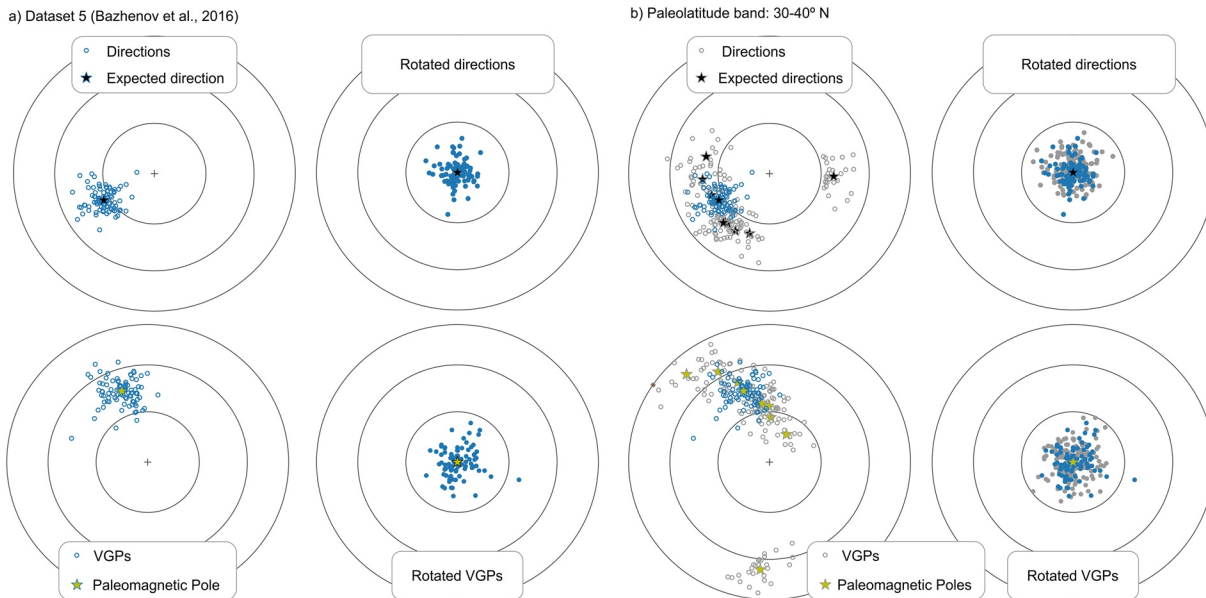
Figure 1. Rotation and grouping of directions and VGPs. (a) An example of a data set (Bazhenov et al., 2016). (b) Grouping paleodirections and VGPs from the paleolatitude band of 30°N –40°N.

As we considered the most simplified GAD versions of the GGP model (like BCE19 and TK03) or the covariant GAD model (like BB18), then zonal and equatorial symmetries are expected. Thus, opposite latitude bands could be joined, as done by Tauxe & Kent (2004) and Brandt et al. (2020).

The expected direction for each data set (black stars in Figures 1a and 1b) was calculated from the paleomagnetic pole, by the following sequence of steps:

1. Calculating VGPs from the published directions of the data set.
2. A mean paleomagnetic pole is determined using the VGPs selected using the iterative cutoff angle of Vandamme (1994).
3. An expected direction (D_{exp}, I_{exp}) is calculated from the paleomagnetic pole.

This procedure helps to avoid the effect of asymmetric directional distributions that result in an angular difference between the mean direction and the expected direction (Brandt et al., 2020). For each data set, the directions were rotated to take the expected direction to the projection's origin (with dec = 0°, inc = 90°). Then they were grouped with other rotated data sets of the same paleolatitude band. For each band, the representative paleolatitude corresponds to the average of the paleolatitudes of the data sets included in the band.

The paleolatitude of each data set was determined using the GAD equation:

$$\tan I_{exp} = 2 \tan \lambda, \tag{7}$$

where I_{exp} is the expected inclination and λ is the paleolatitude corresponding to the data set. This determination has the same result as the approach described by Doubrovine et al. (2019), which is also based on the mean paleomagnetic pole.

In a difference from the usual procedures in paleomagnetic reconstructions (e.g., Gallo et al., 2017; Torsvik et al., 2012) that use pre-defined paleo-reconstructions, mean paleomagnetic poles, and rotation angles, we preferred to calculate paleolatitudes individually per data set (described above) to avoid problems related to age uncertainties, the best choice of rotation poles to adjust tectonic blocks, and the choice between Pangea model A or B (Irving, 1977).

2.4. Analysis and Modeling of Directional Distributions

The directional analysis was based on the shape and scale of distributions following Brandt et al. (2020). The statistic parameters used are the standard deviations σ_E and σ_N (Equations 8 and 9) of equal-area coordinates x_E (east-west) and x_N (north-south) of the rotated directional distributions:

$$\sigma_E = \sqrt{\frac{\sum_{i=1}^{N}\left(x_{Ei} - \overline{x_E}\right)^2}{N-1}}; \overline{x_E} = \frac{\sum_{i=1}^{N} x_{Ei}}{N} \tag{8}$$

$$\sigma_N = \sqrt{\frac{\sum_{i=1}^{N}\left(x_{Ni} - \overline{x_N}\right)^2}{N-1}}; \overline{x_N} = \frac{\sum_{i=1}^{N} x_{Ni}}{N} \tag{9}$$

$$\sigma_{EC}^2 = \left\langle \sigma_E \right\rangle^2 - \frac{r^2}{2} \tag{10}$$

$$\sigma_{NC}^2 = \left\langle \sigma_N \right\rangle^2 - \frac{r^2}{2} \tag{11}$$

$$r = \sqrt{1 - \overline{\alpha_{63}}} \tag{12}$$

Here N is the number of sites, σ_{EC} and σ_{NC} are the standard deviations corrected for within sites errors ($\frac{r^2}{2}$) and r is the radius of the equal-area projection of the mean angle α_{63} of the set of directions. The 95% confidence limits of σ_{EC} and σ_{NC} were determined from 1,000 bootstrapped samples.

The latitudinal dependence of σ_E and σ_N can provide useful diagnostics for the validity of a given GGP model, as both shape (elongation) and scale of the distributions vary with location. Therefore, we used these measures (σ_E and σ_N) for the Kiaman database, using different selection criteria (Cromwell et al., 2018; Tauxe & Kent, 2004) to test whether the existing GGP models are valid for this superchron, as well as for searching a new GGP model for this time interval. For a zonal GGP model with a GAD mean, the latitudinal dependence σ_E and σ_N is symmetric about the Equator and independent of polarity, allowing the use of a simplified GGP model (like TK03) for the geological past when the polarity or the paleo-hemisphere are often unknown. The same can be said for a covariant GGP model with a mean GAD (like BB18, Bono et al., 2020), which can be considered almost invariant with longitude and symmetric to the Equator. Thus, we searched for the best fitting simplified GGP model $m = \left(\alpha, \beta, \overline{g_1^0}\right)$ like TK03 and a covariant version like BB18 (with the correlations included as specified in Table 3 from Bono et al., 2020). The models were found by the minimization of the squared differences between theoretical predictions and directional standard deviations (σ_{EC}, σ_{NC}) estimated for the Kiaman database.

The mean dipole strength used for modeling was determined using the VDM data of ages between 267 and 318 Ma. The research included the PINT database (Biggin et al., 2010, version 2015.05) and The World Paleointensity Database from Borok Geophysical Observatory. For this interval of age, the databases are fundamentally the same, with only one reference of difference. Therefore, we used Borok's database, which had more data included.

A mean of VDMs (VDM $= 7.47 \times 10^{22}$ Am^2) was calculated using 177 paleointensity data (Bolshakov et al., 1989; Briden, 1966; Cottrell et al., 2008; Garcia et al., 2006; Harcombe-Smee et al., 1996; Krs, 1967; Schwarz & Symons, 1969; Senanayake & McElhinny, 1983; Shcherbakova et al., 2005; Solodovnikov, 1992a, 1992b; Thomas et al., 1995, 1997; Usui & Tian, 2017). It is important to note that many of
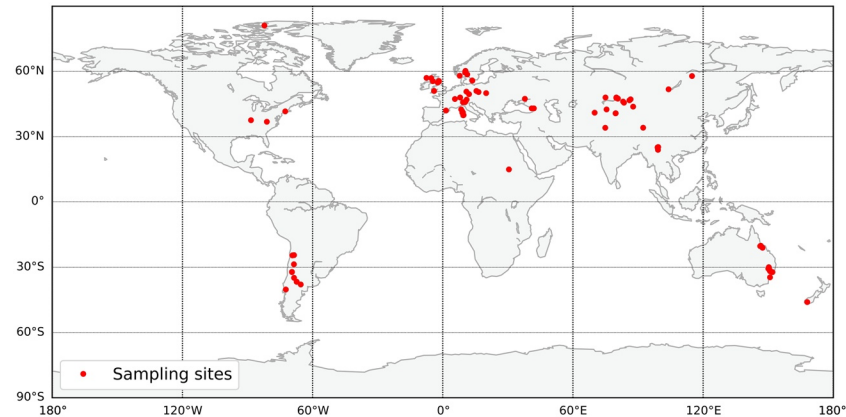
Figure 2. Distribution of the paleomagnetic sampling sites selected for the PDKRS.

the data included in this average do not pass the common paleointinsity reliability criteria, so, depending on the filtering process the mean result can change significantly.

The mean *VDM* was used to determine the mean dipole value of $\overline{g_1^0}$ = 28.9 μT using Equation 13.

$$g_1^0 = \frac{\mu_0 VDM}{4\pi R_E{}^3},$$

(13)

where μ_0 is the magnetic vacuum permeability and R_E is the radius of the Earth. We should however note that since we are only interested in directional shape here, only the ratio of α to $\overline{g_1^0}$ matters.

We used the ratio $E' = \sigma_{NC}{}^2/\sigma_{EC}{}^2$ as a measure of the elongation of distributions along the N-S direction and the area given by the product $A_{dir} = \sigma_{NC}\sigma_{EC}$ to characterize the overall dispersion (following Brandt et al., 2020). All calculations were performed in Python with the help of functions available from the PMAG-PY package (Tauxe et al., 2016) and the directional PSV predictions of simplified GGP models derived by Brandt et al. (2020) and available at github.com/danielebrandt/BCE19-dirPSV.

3. The Paleomagnetic Database for the Kiaman Reversed Superchron

The flexible criteria outlined in Section 2.1 were used to build the largest possible directional database for the Kiaman, in contrast to the precursory filtering for high-quality data considered in other recent compilations (Cromwell et al., 2018; Doubrovine et al., 2019; Oliveira et al., 2018). This procedure resulted in a database with 1,459 reliable igneous directions (available at MagIC database as PDKRS, earthref.org/MagIC/16854) corresponding to 91 paleomagnetic poles (data sets) of which 62 (1,017 directions) are based solely on extrusive rocks. Figure 2 shows the sampling locations and Table 1 summarizes the paleomagnetic poles. Below we also consider the effects of adding further quality criteria to filter the data.

As outlined in Section 2.1 (criterion 8), the highest and lowest Fisher's (1953) precision K parameter was evaluated for latitude bands with more than 50 VGPs, and resulted in maximum and minimum of K_{max} = 64 and K_{min} = 14. These values are higher than those given by Deenen et al. (2011) for all ages and thus produce smaller upper and lower bounds for A_{95} (blue curves in Figure 3a). The new A_{95} envelope for the Kiaman database (light blue area delimited by blue curves, Figure 3a), excludes seven data sets (74 directions), five with limited PSV sampling, and two with large scatter probably due to non-PSV sources. These data sets are indicated by asterisks in Table 1. The resulting number of site level directions is reduced from 1,459 to 1,385, ~95% of the original. Figure 3b shows the numbers of data remaining as a function of absolute latitude (blue columns). The excluded A_{95} are mostly near to the lower limit (Figure 3a), the use

Table 1
Compiled Kiaman Paleomagnetic Results Indicating the Excluded Studies (*) Based on the Above Criteria (More Results in Table S1)

N_{POLE}	Geologic unit	T.	N_{ig}	Lon_S	Lat_S	Dec(°)	Inc(°)	Plat	S_F (S_{FL}, S_{FU})	Age_L	Age_U	Rev	DC	References
1*	Alum Mountain Volcanics	E	18	152	−32.2	27.5	88.8	−87.5	40.3 (33.6,46.2)	270	277.5	100	5	Shaanan et al. (2015)
2*	Bulgonunna Volcanics	E/I	12	147.4	−21	203.5	79.0	−68.8	28.6 (19.1,36.1)	293	305	100	4	Lackie et al. (1992)
3	Gerringong Volcanics	E	17	150.8	−34.6	174.4	78.3	−67.5	17.5 (13.5,20.8)	264.7	265.4	71	5	Belica et al. (2017)
4	Boggabri Volcanics	E	6	150.1	−30.6	176.5	78.2	−67.2	10.8 (6.2,13.3)	260	299	100	4	Klootwijk (2003)
5	Currabubula F. (W. S.	E	23	150.6	−31.2	233.8	77.8	−66.7	20.2 (13.1,25.5)	304	315	100	4	Opdyke et al. (2000)
6	Mount Leyshon Intrusive C.	I	34	146.3	−20.3	196.4	77.7	−66.5	17.8 (14.2,21)	279	287	100	4	Clark and Lackie (2003)
7	Lark Hill Formation	E	8	150.3	−29.9	213.9	75.8	−63.1	6.1 (1.8,9.8)	306	314	100	4	Klootwijk (2002)
8	Tuckers Igneous Complex	I	46	146.6	−20.1	183.6	75.3	−62.3	17.6 (13.9,20.6)	283	291	100	4	Clark and Lackie (2003)
9	Lago Ranco Granites	I	7	287.7	−40.2	139.0	74.7	−61.4	24.5 (16.4,31.2)	297	307	86	4	Beck et al. (1991)
10	Werrie Basalt	E	6	150.5	−31	158.3	74.5	−61.1	21.8 (8.2,31.2)	271	299	100	4	Lackie and Schmidt (1993)
11	Rocky Creek	E	9	150.3	−30.2	203.8	73.6	−59.5	18.4 (6.8,26.8)	310	315	100	4	Opdyke et al. (2000)
12	Base Currabubula F. (W. B.	E	11	150.7	−31.3	219.7	73.3	−59.0	10.9 (4.7,16.1)	302	318	100	4	Klootwijk (2003)
13	Werrie Basalt	E	9	151	−31.9	200.2	72.9	−58.4	23.7 (15.2,31.4)	260	299	100	4	Klootwijk (2003)
14	Base Currabubula F. (K. B.	E	9	150.8	−31.7	209.2	69.3	−52.9	12 (6.9,16.1)	302	318	100	4	Klootwijk (2003)
15	Woniusi F. (Baoshan Terrane	E	6	99	25	153.5	67.9	−50.9	24.5 (20.8,28.9)	273.1	280	100	4	Xu et al. (2015)
16	Upper Choiyoi Group	E	40	291.4	−34.8	169.1	66.3	−48.8	12.9 (10.6,14.8)	260	269	53	5	Domeier et al. (2011c)
17	Top Currabubula F. (W. Basin	E	18	150.6	−31.3	243.7	65.9	−48.2	10.8 (6.9,14.1)	302	318	100	4	Klootwijk (2003)
18	Woniusi Form. Loc Yongde	E	6	99.2	23.9	294.9	64.2	−45.9	13.5 (9.1,16.9)	299	318	100	4	Huang and Opdyke (1991)
19	Woniusi Formation	E	14	99.3	25.2	241.7	63.7	−45.3	21 (17.1,24.7)	270.6	280	100	5	Ali et al. (2013)
20	Rincon Blanco	E	9	291.4	−28.6	187.7	63.3	−44.9	14.7 (7.6,20.5)	271	318	100	4	Geuna and Escosteguy (2004)
21	Woniusi Form. Baoshan	E	13	99.3	25.2	208.8	61.5	−42.6	17.3 (14.8,19.7)	299	318	100	4	Huang and Opdyke (1991)
22	Sierra Chica	E	35	294.5	−37.9	169.0	61.3	−42.4	8.7 (6.3,10.8)	261	264.6	89	5	Domeier et al. (2011b)
23	Tambillos Formation	E	16	290.5	−32.2	175.6	60.9	−42.0	13.4 (9.2,17.1)	271	285	100	3	Rapalini and Vilas (1991)
24	La Tabla Formation	E	10	290.7	−24.5	136.4	59.1	−39.9	8.8 (4.4,10.9)	251	318	100	4	Jesinkey et al. (1987)
25	Cas Formation	E	10	291.5	−24.4	143.8	57.0	−37.6	17.4 (11.2,23.5)	299	318	50	4	Jesinkey et al. (1987)
26	Panjal Traps of NW India	E	14	74.9	34	135.0	56.2	−36.8	23.5 (16.9,29.4)	286	292	100	5	Stojanovic et al. (2016)
27	Woniusi F. (Baoshan Terrane	E	13	99	24.9	232.7	55.6	−36.2	16.2 (12.6,19.8)	273.1	280	100	4	Xu et al. (2015)
28	Takitimu Mountains	E	8	168	−46	262.6	45.7	−27.1	4.5 (1.3,8.5)	276	284	100	4	Haston et al. (1989)
29	Woniusi Formation	E	8	99.1	24.9	124.4	45.6	−27.1	7.6 (5.3,9.5)	270.6	280	100	5	Ali et al. (2013)
30	Portezuelo del Cenizo	E	17	290.5	−32.1	248.4	41.0	−23.5	15 (10.5,19.3)	265	285	100	3	Rapalini et al. (1989)
31	Jebel Nehoud Ring Complex	I	8	30.5	14.9	147.1	40.0	−22.8	6.4 (2.5,9.4)	278	282	100	4	Bachtadse et al. (2002)

Table 1
Continued

N_{POLE}	Geologic unit	T.	N_{ig}	Lon_S	Lat_S	Dec(°)	Inc(°)	Plat	S_F (S_{FL}, S_{FU})	Age_L	Age_U	Rev	DC	References
32	Qiangtang Kaixinling group	E	14	92.4	34.1	219.8	39.9	−22.7	17.7 (13.4,21.8)	295	298.8	64	4	Song et al. (2017)
33	South Carolina Piedmont	I	20	278.9	36.8	160.2	22.1	−11.5	11.9 (9.3,14.3)	265	295	100	3	Dooley (1983)
34	Middletown Pegmatites	I	5	287.4	41.6	164.9	21.4	−11.1	7.4 (4.6,10.3)	252	262	100	2	De Boer and Brookins (1972)
35	H. W-P. Sill and H. Dyke	I	47	357.7	54.9	188.7	4.2	−2.1	8.6 (7,10.3)	292	297	100	4	Liss et al. (2004)
36	Cinto Volcanic Complex	E	5	8.5	42.5	165.4	4.0	−2.0	9.6 (4.1,13.5)	251	299	100	2	Westphal et al. (1976)
37	Rotliegendes S. (Thuringer F.	E	9	10.9	50.7	194.1	1.4	−0.7	14.1 (8,19.8)	271	299	100	3	Mauritsch and Rother (1983)
38	Volcanic rocks of Moissey	E	7	5.6	47.3	189.8	1.4	−0.7	6.2 (3.9, 8)	276	284	100	4	Thompson et al. (1986)
39	Sardinia Dykes	I	11	9.3	41.1	132.7	−1.7	0.8	9.2 (5.8,11.9)	251	299	100	4	Vigliotti et al. (1990)
40	NW Sardinia Ignimbrites	E	6	9	41	142.3	−1.8	0.9	10.3 (4.4,14.6)	251	299	100	3	J. D. Zijderveld et al. (1970)
41	Holy Island Sill and Dyke	I	20	358.2	55.6	185.1	−2.1	1.0	7.1 (4.5,9.2)	292	297	100	4	Liss et al. (2004)
42	Pyrenees Andesites	E	10	1.5	42	169.4	−3.0	1.5	8.9 (5.1,12)	271	299	100	3	Van Dongen (1967)
43*	Argyll Dykes	I	15	354.7	56.9	180.3	−4.0	2.0	6.1 (3.6,8.1)	316	324	100	3	Esang and Piper (1984)
44	Dykes of Sardinia (C-E	I	6	9.6	39.9	92.0	−4.8	2.4	10.1 (4.6,13.6)	289	298	100	4	Aubele et al. (2014)
45	Lower Silesia Volcanics	E	12	15.5	51	197.3	−5.8	2.9	13.3 (9.2,16.7)	271	299	100	2	Birkenmajer et al. (1968)
46	SE Sardinia	E	27	9.5	39.8	85.2	−7.7	3.9	12.7 (10.1,15.1)	304	312	100	3	Edel et al. (1981)
47	Bolzano Volcanics	E	25	11	47	163.8	−11.8	6.0	15 (11.9,18.2)	271	299	100	2	Dietzel (1960)
48	Corsica Dykes	I	11	9	41.6	134.7	−12.0	6.1	8.3 (4.4,11.8)	251	299	100	4	Vigliotti et al. (1990)
49	Bohemian Massif	I	8	12.1	49.6	200.0	−12.2	6.2	9.1 (6.3,11.6)	275	280	100	3	Soffel and Harzer (1991)
50	Lower Silesia Volcanics	I/E	8	16.5	50.5	195.4	−12.9	6.5	13.4 (7.7,18.4)	299	307	100	2	Birkenmajer et al. (1968)
51*	Southern Illinois	I	6	271.6	37.5	163.1	−14.9	7.6	4.3 (3, 5.1)	260	270	100	5	Domeier et al. (2011a)
52	Black Forest	I	18	8	48	189.9	−15.3	7.8	9.6 (6.6,11.9)	271	299	100	3	Konrad and Nairn (1972)
53	Scania Dolerites	I	13	13.6	55.8	199.5	−15.3	7.8	10.4 (7.5,13.5)	250	350	100	3	Bylund (1974)
54	Western Southern Alps	E	13	9.3	45.8	139.1	−16.3	8.3	8 (5.8,10.1)	271	299	100	3	Heiniger (1979)
55	Krakow Volcanics	E	11	20	50	205.2	−16.9	8.6	-	271	299	100	2	Birkenmajer and Nairn (1964)
56*	Ny-Hellesund Dykes	I	10	7.8	58	201.3	−18.4	9.5	2.3 (0.6,3.9)	272	284	100	2	Halvorsen (1970)
57	Exeter Lavas	E	7	356	51	193.7	−19.6	10.1	7 (4.6, 8.7)	279	291	100	3	Cornwell (1967)
58	Lower Collio and Auccia	E	5	10.2	45.8	135.6	−21.8	11.3	21.3 (9.1,31)	271	299	100	3	J. D. A. Zijderveld and De Jong (1969)
59	Ukrainian Shield	I	19	37.9	47.4	204.4	−24.5	12.8	12.6 (10.4,14.7)	280	285.2	100	4	Yuan et al. (2011)
60	Sakmarian stage Aksaut River	E	41	41	43	235.3	−25.1	13.2	11.9 (10.3,13.5)	284	295	100	3	Solodovnikov (1992a)
61*	Exeter Lavas	E	5	356	51	197.4	−25.2	13.2	5.2 (2.7,6.8)	281	291	100	3	J. D. A. Zijderveld (1967)
62	Southern Alps Volcanics	E	7	10.5	46.2	151.4	−25.9	13.6	8.5 (6.5,10.3)	276	284	100	4	Muttoni et al. (2003)

Table 1
Continued

N_{POLE}	Geologic unit	T.	N_{ig}	Lon$_S$	Lat$_S$	Dec(°)	Inc(°)	Plat	S_F (S_{FL}, S_{FU})	Age$_L$	Age$_U$	Rev	DC	References
63	A. Sill, H. G., St. O. C. Dyke	I	17	358.3	55.4	198.9	−26.3	13.9	11 (5.1,15.4)	292	297	100	4	Liss et al. (2004)
64	Northern Caucasus	E	22	42	43	249.2	−26.5	14.0	7.9 (5.8,10)	270.6	299	100	3	Bolshakov et al. (1989)
65	Mauchline Lavas	E	5	355.4	55.5	192.4	−26.7	14.1	10.3 (2.8,14.7)	290	305	100	3	Harcombe-Smee et al. (1996)
66	Barra Dykes	I	9	352.5	57	183.8	−27.0	14.3	13.3 (8.7,17.5)	251	299	100	4	Piper (1992)
67	Oslo Gr.- Vestfold	E	49	10.3	59.5	201.0	−36.2	20.1	9.3 (7.7,10.7)	284	300	100	5	Haldan et al. (2014)
68	Bohuslan Dykes	I	16	11.3	58.6	194.6	−37.8	21.2	14.2 (9.5,18.5)	271	299	100	3	Thorning and Abrahamsen (1980)
69	Scania melaphyres	I	8	13.7	55.7	192.1	−39.2	22.2	14.1 (10.1,17.8)	250	285	100	3	Bylund (1974)
70	Lunner dykes	I	25	10.5	60.3	196.8	−40.1	22.8	7.5 (4.7,10.1)	268.3	273.7	100	5	Dominguez et al. (2011)
71	Oslo Gr.- Krokskogen	E	55	10.4	60	208.1	−40.4	23.0	9.8 (8.3,11.3)	276	292	100	5	Haldan et al. (2014)
72*	Bakalin Fm. (B)	E	8	80.7	47.5	237.0	−48.1	29.2	3.8 (1.7,5.6)	251	260	100	4	Levashova et al. (2003)
73	Harlegiawu and Karlagang	E	14	86.1	46.7	166.9	−48.8	29.7	12.7 (7.7,16.4)	271	318	100	4	Li et al. (1991)
74	Biyoulitie Super Fm.	E	21	79.7	40.7	222.5	−49.9	30.7	9.6 (7.4,11.8)	271	299	100	4	Sharps et al. (1989)
75	Northern Tien Shan	E	7	75.5	42.5	210.2	−50.1	30.9	10.1 (4.4,14)	251	299	100	3	Audibert and Bazhenov (1992)
76	Bakalin Fm. (A)	E	8	80	47.8	265.0	−50.6	31.3	8 (4.8,10.7)	251	260	100	4	Levashova et al. (2003)
77	Tarim large igneous province	E	11	79.7	40.8	221.7	−51.0	31.7	13.2 (7.9,18)	284.8	291	100	5	Usui and Tian (2017)
78	Maitas Formation	E	19	75	48	219.3	−51.3	31.9	9 (5.5,11.6)	251	275	100	4	Abrajevitch et al. (2008)
79	Koldar Formation	E	15	80	48	285.4	−51.5	32.2	12.3 (9.1,15)	275	305	100	4	Abrajevitch et al. (2008)
80	Molaoba Formation	E	12	83.1	46.1	198.0	−52.3	32.9	9.7 (7.3,12.1)	299.3	308.7	100	4	Yi et al. (2015)
81	Uzbekistan Igneous rocks	E	26	70	41	92.5	−52.4	33.0	10.8 (8.1,13.3)	299	318	100	3	Solodovnikov (1992b)
82	Ayaguz Formation	E	32	80.7	47.5	249.1	−53.8	34.4	13.5 (10.4,16.2)	280.7	285.3	100	4	Menzo (2013)
83	Bakaly	E	88	80.7	47.5	241.8	−56.5	37.0	9.9 (8.6,11.2)	282.8	289.9	100	4	Bazhenov et al. (2016)
84	Junggar Dykes	I	23	83.5	45.6	186.6	−56.8	37.4	19.9 (17.1,22.6)	271	318	100	4	Li et al. (1989)
85	Liushugou Dykes	I	7	87.8	43.8	226.0	−56.8	37.4	18.5 (8.4,26)	271	318	100	4	Li et al. (1991)
86	Hoboksar	E	16	86.6	47.2	153.7	−59.5	40.3	19.8 (14.4,24.3)	271	318	100	4	Li et al. (1991)
87	Esayoo Formation	E	12	277.8	81.1	125.6	−61.6	42.8	11.1 (7.2,14.3)	271	299	92	3	Wynne et al. (1983)
88	Angara-Vitim batholith	I	8	114.9	57.9	331.6	−79.7	70.0	-	296.1	305.9	100	4	Shatsillo et al. (2014)
89	Mafic dykes – Sib.	I	5	104.1	51.8	269.4	−84.5	79.1	11.7 (1.1,19)	271	279	100	5	Pisarevsky et al. (2006)
90	El Centinela I	E	25	292.7	−36.6	142.7	62.8	−44.3	11.7 (9.1, 14.2)	290	310	100	4	Tomezzoli et al., 2018
91	El Centinela II	E	15	292.7	−36.7	159.2	44.0	−25.8	6.7 (5.6, 7.8)	265	287	100	4	Tomezzoli et al., 2018

Note. N_{POLE}: number of data set; T.: type of rock (I: intrusive, E: extrusive); N_{ig} (number of igneous sites); Lon$_S$ and Lat$_S$: longitude and latitude of the sampling site; Dec and Inc: declination and inclination of expected direction; Plat: paleolatitude, S_F (S_{FL}, S_{FU}): VGP scatter with limits of confidence; Age$_L$ and Age$_U$: interval of age; Rev: % of reversed directions of the data set; DC: demagnetization code (McElhinny and Lock, 1996).

of the original limits (gray dashed curve) defined by Deenen et al. (2011), instead of that presented here, would mainly exclude data sets with lower A_{95} and higher number of sites (13 data sets or 245 directions).

If we consider only extrusive rocks as the best rock type for getting an instantaneous record of the geomagnetic field, as commonly used for PSV studies (e.g., McElhinny & McFadden, 1997), the total number of spot
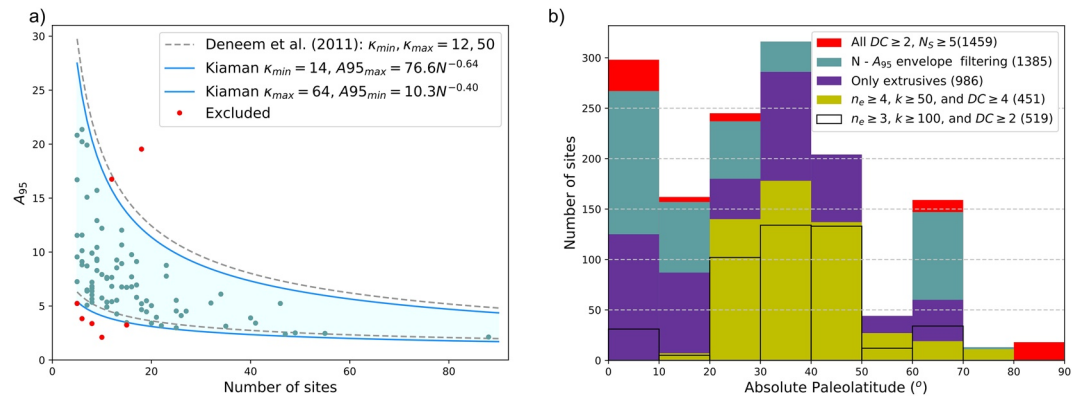
Figure 3. (a) Filtering the data set by using the paleomagnetic pole confidence angle A_{95} limits criteria. Dashed lines are the A_{95} limits from Deenen et al. (2011) and the blue curves are the limits defined for the Kiaman database. (b) Number of paleomagnetic sites per bands of 10° in paleolatitude; colors discriminate the filtering process: red: all data; green: N-A_{95} envelope; purple: only extrusives; yellow: extrusives and filtering following Cromwell et al. (2018) ($n_e \geq 4$, $k \geq 50$, and DC ≥ 4); empty bar with black contour: extrusives and the filtering following Tauxe and Kent (2004) ($n_e \geq 3$ and $k \geq 100$).

readings is cut down to 986 (~67% of the whole database; purple columns in Figure 3b), and the range of well-sampled latitudes becomes 0°–50° instead of 0°–70° considering all data.

Two additional filtering procedures can be applied to the PDKRS: 1) the removal of directions based on less than three specimens and with statistical precision k (Fisher, 1953) less than 100, as implemented by Tauxe and Kent (2004) for the 0–5 Ma lava data; 2) the removal of data sets with DC < 4 (McElhinny & Lock, 1996), and directions with $n_e < 4$ and $k < 50$, used by Cromwell et al. (2018) for the last 10 Ma lava database. After these two filtering processes, the number of results (empty and yellow bars, respectively, in Figure 3b) is significantly reduced, leaving only the three consecutive bands of latitudes from 20° to 50° with sufficient numbers of directions (approximately 100) for a credible analysis, representing only a 30° slice of the hemisphere. Because of the limited size of the Kiaman database, which is much smaller than for 0–10 Ma (Cromwell et al., 2018), we decided to maintain our initial flexible filtering. However, the results from the extrusive and intrusive rocks are considered separately and compared. We also evaluate the effects of imposing further stringent criteria described above.

4. VGP Scatter and Model G-Type Results

The VGP scatter S_F was determined for each data set. Data from the Northern and Southern Hemispheres are combined. Inter-Hemispherical comparisons are not possible as the sampled paleolatitude intervals are not the same for both hemispheres, precluding the investigation of any asymmetric behavior of the field. S_F values follow a general trend of increasing dispersion with paleolatitude (Figure 4).

The shape parameters (a and b) from Model G (McFadden et al., 1988) were calculated for the whole database and various filtered subsets (Figure 4 and Table 2). Inserting intrusive records into the analysis does not significantly influence the results, but it is worth considering that the whole data set includes fewer intrusive records than extrusive records; they are also unequally distributed across the latitude bands. It is not evident that the intrusive data sets produce less scatter than the extrusive as might be anticipated from slower cooling; maybe this is a characteristic of this superchron. However, to avoid any possible bias due to the intrusive records, we will proceed with analyses using only extrusive data.

Applying cutoffs to the number of sites per study ($N_S \geq 10$ and $N_S \geq 20$) produces similar results to using only extrusives with lower cutoff ($N_S \geq 5$). The confidence region based on bootstrap sampling becomes smaller as the N_S increases. However, the decreasing size of the data set available for resampling does not necessarily mean improved confidence in the result. The greatest changes in the shape parameters occur after applying a filter based on intrasite statistics (modern filters following Cromwell et al., 2018 and Tauxe
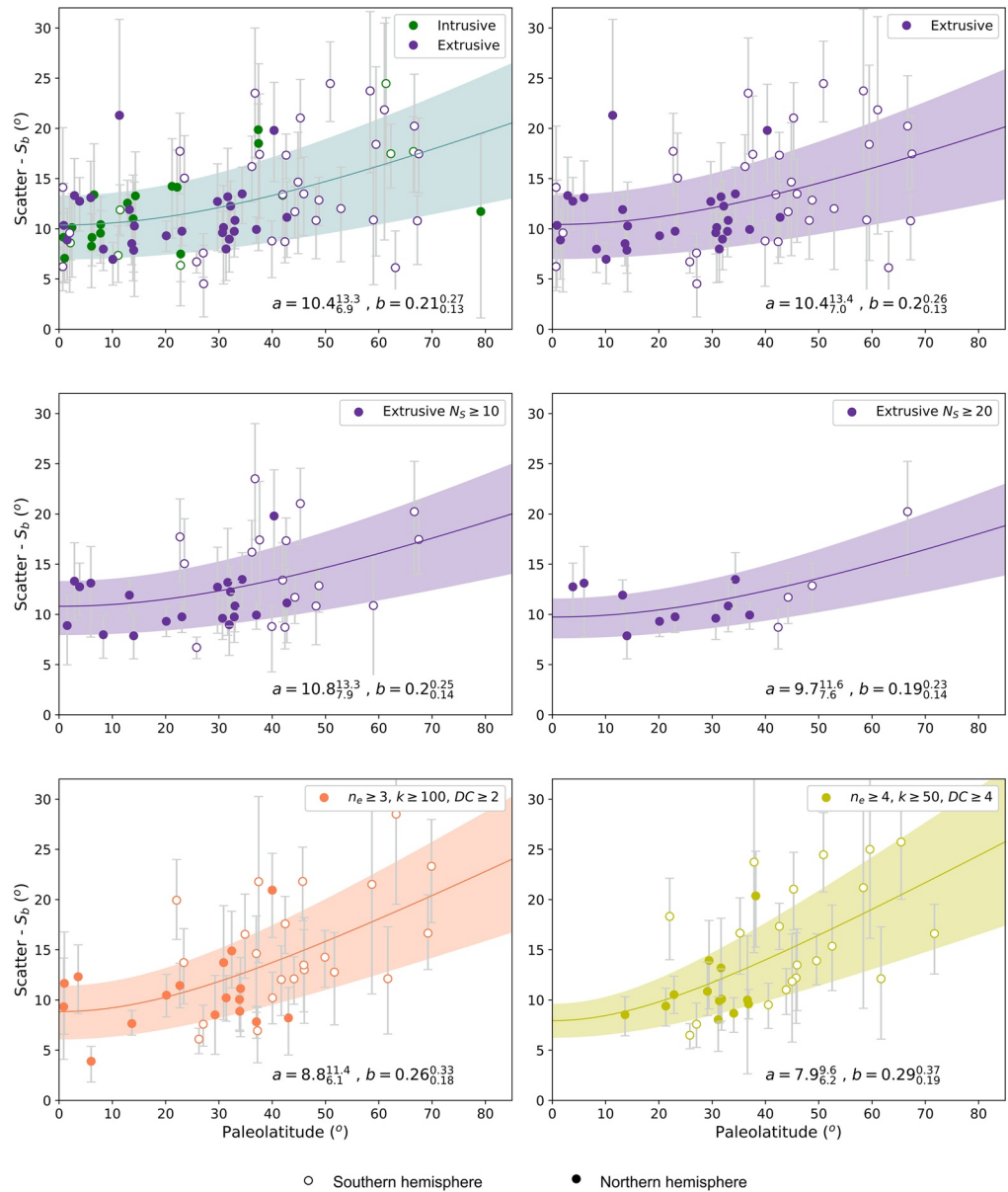
Figure 4. VGP scatter results per data set. Closed (open) symbols are Northern (Southern) Hemisphere data. Green: intrusive; purple: extrusive; coral: extrusive database filtered using $n_e \geq 3, k \geq 100, DC \geq 2$ (as Tauxe and Kent, 2004); and yellow: extrusive filtered using $n_e \geq 4, k \geq 50, DC \geq 4$; a and b are the fitted shape parameters from Model G.

& Kent, 2004), producing the lowest values for a the equatorial VGP dispersion, and the highest values for b which controls the latitudinal dependence in VGP dispersion.

5. Shape and Scale of Directional PSV During Kiaman Times

The directional PSV analyses are related to directions grouped using the latitude bands as described in Section 2.3. This procedure was adopted considering that all igneous units within a given latitude band should have sampled approximately the same overall behavior of the geomagnetic field during the Kiaman superchron. This premise is reasonable since we considered only zonal and equatorially symmetric PSV models in this study.

Table 2
Results of Shape Parameters for Kiaman Databases Using Different Filtering Processes

Kiaman database filtering	N_d	N_S	N_{SV}	a	b	$\chi^2_{S_F}$	L_{S_F}	Reference
All igneous	82	1,366	1,348	$10.4^{13.3}_{6.9}$	$0.21^{0.27}_{0.13}$	503	2.48	This study
Extrusives	58	975	967	$10.4^{13.4}_{7.0}$	$0.20^{0.26}_{0.13}$	417	2.68	This study
Extrusives ($N_S \geq 10$)	37	825	818	$10.8^{13.3}_{7.9}$	$0.20^{0.25}_{0.14}$	283	2.77	This study
Extrusives ($N_S \geq 20$)	14	509	503	$9.7^{11.6}_{7.6}$	$0.19^{0.23}_{0.14}$	53.8	1.96	This study
Extrusives ($N_S \geq 5, n_e \geq 3, k \geq 100, DC \geq 2$).	9	451	449	$8.8^{11.4}_{6.1}$	$0.26^{0.33}_{0.18}$	330	2.91	This study
Extrusives ($N_S \geq 5, n_e \geq 4, k \geq 50, DC \geq 4$)	33	519	516	$7.9^{9.6}_{6.2}$	$0.29^{0.37}_{0.19}$	247	2.73	This study
Igneous rocks ($N_S \geq 10, DC \geq 4$)	9	336	331	$9.4^{10.9}_{7.5}$	$0.27^{0.29}_{0.22}$			(Oliveira et al., 2018)

Note. N_d: number of data sets, N_s: total number of sites; N_{SV}: number of sites after iterative cutoff; the misfit $\chi^2_{S_F}$ and normalized misfit $L = \sqrt{\chi^2 / N}$ was performed following Doubrovine et al. (2019) and Bono et al. (2020).

Figure 5 shows the stereograms of directions rotated with the expected direction at the origin for eight latitude bands from 0° to 70°, with data from the Southern (blue) and Northern (green) Hemispheres merged. The paleomagnetic data sets originate from paleolatitudes ranging from 70°S to 50°N. The majority of the data from absolute paleolatitudes 0°–40° comes from the Northern Hemisphere. Those in the bands 40°–70° data are mostly from the Southern Hemisphere. The most elongated distribution is the equatorial (0°–10° paleolatitude band) and the few southern directions belonging to this group (blue circles) seem to follow the same tendency. For the other latitude bands in both hemispheres, distributions display a more circular shape.

The directional shape statistics for the Kiaman database (only extrusive data) are shown in Figure 6a (intrusive and igneous are shown in Figure S1). For comparison, the figure also shows the predicted values of σ_E, σ_N, E', and A_{dir} determined for TK03 and the recent BCE19 models (Brandt et al., 2020).

The Kiaman results show consistently lower overall variability, A_{dir}, than the TK03 and BCE19 models at all latitudes. Values σ_N are consistently lower and disagree with the TK03 and BCE19 predictions. σ_E is also lower and incompatible with the TK03 and BCE19 predictions in almost all latitude bands. The elongation E' is compatible with TK03 and BCE19 models only at Equatorial paleolatitudes, for latitudes higher than 10° it decreases to 1 (circular shape). If the data of intrusive rocks were inserted in the results and all types of igneous records were considered (light blue symbols at Figure S1a) the overall variability and elongation at equatorial paleolatitudes would be diminished. The huge step of elongation between the equatorial band ($E \sim 3$) and 10°–70° ($E \sim 1$) seen at only-extrusive results (purple symbols) would shrink, finding a more suitable variation of elongation with paleolatitude ($E \sim 2.2$ to $E \sim 1$, light-blue symbols). However, despite a greater number of data and a smoother result (at least in terms of elongation), the inclusion of intrusive records would imply doubt about how much the cooling time of the considered rocks affects the record of the geomagnetic field. A sampling site from slowly cooled rocks has the record of rapid PSV removed, being the site result in an average over time. Therefore, in order to have the most robust PSV results, we use only extrusive rocks.

5.1. Reliability of PSV Directional Results

The directional PSV results for the Kiaman reveal distinct properties when compared to the recent field results. The shape and dispersion of the direction distributions all over the globe are quite different from those observed for the past 10 million years (Brandt et al., 2020), which are compatible with the models TK03 and BCE19. Thus, it is important to assess the reliability of the results in the older Kiaman context. In contrast to the PSV10 (Cromwell et al., 2018), the Kiaman results are based on the direction distributions of
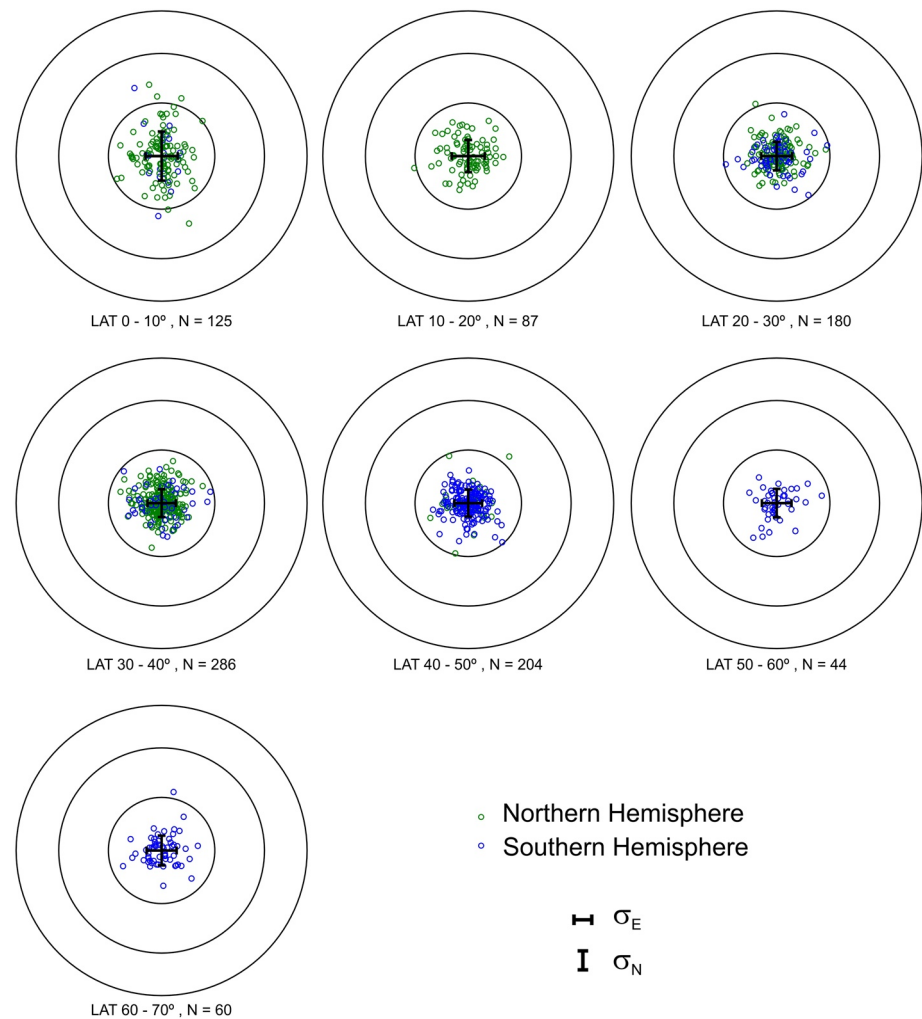
Figure 5. The PDKRS considering only extrusive rocks; blue (green) is related to Southern (Northern) Hemisphere data. Circles are directions rotated with the expected direction from each data set at the origin (dec = 0°, inc = 90°). From the left top to bottom are bands of paleolatitudes from 0° to 70°. The black lines show the σ_E and σ_N standard deviations determined for each band.

the paleo-reconstructed data sets described in Section 3. Ill-determined declinations (paleo-meridians) may contribute to a circular distribution of the merged directional data. Inaccurate determination of the expected inclinations may lead data to fall into an incorrect paleolatitude band. These sources of error are absent in the PSV10 results. Moreover, the filtering applied to the PDKRS is less rigorous than the criteria used for PSV10. Thus, it is worth testing whether the results obtained for the Kiaman superchron arose from the way the data set was constructed. Therefore, we introduce a resampling procedure and some further filtering to test the consistency of the results we obtained. The results are in Figures 6b and 7.

Each data set was randomly resampled by the bootstrap method 1,000 times to test the impact of uncertainty in paleolatitude determinations, and consequently, the corresponding assignment to latitude bands. The resampling may displace a data set from one initial band to a neighboring band. Each resampling run produced the same number of data as the original data, that is, 986 extrusive directions distributed in seven latitude bands (Figure 6b). The dots in the figure represent the produced data, and the bars mark the 95% confidence limits of the resampled distribution.

The resampling process broadened the paleolatitude intervals for each latitude band. However, even with this variation in paleolatitude intervals determinations, the procedure did not reveal any different behavior for the Kiaman results from that previously observed. For latitudes higher than 10°, PSV results from
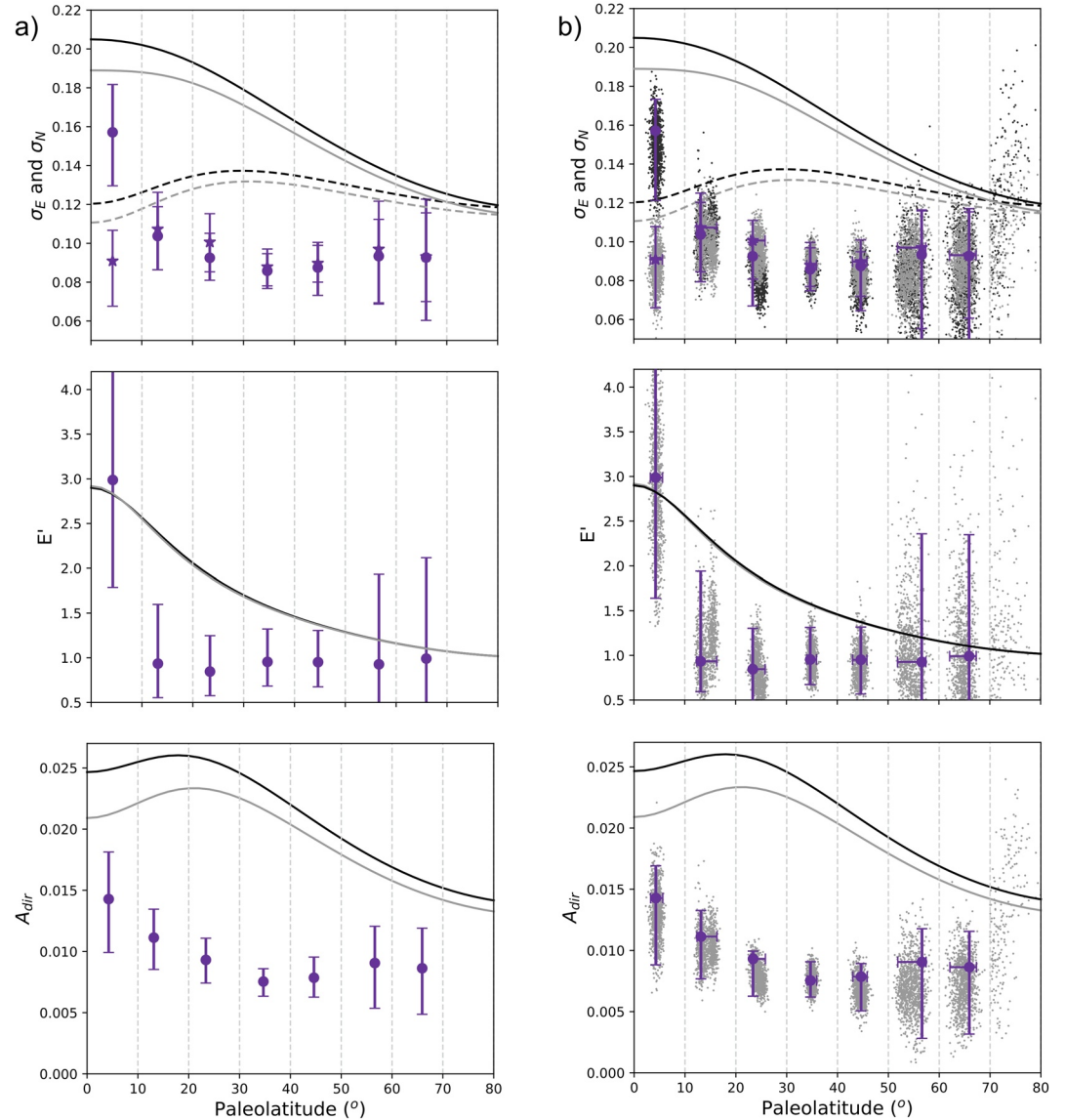
Figure 6. (a) Directional PSV results using 10° bands of paleolatitude from extrusive paleomagnetic data from Kiaman reverse superchron (Table S2); σ_E (stars) and σ_N (circles) are the standard deviation for the x_E and x_N equal-area coordinates from rotated distributions; $E' = \sigma_{N^2}/\sigma_{E^2}$ is the distribution elongation in the N-S direction, and $A_{dir} = \sigma_E \sigma_N$ is the overall variability of the distributions. Black (gray) curves are the predicted values of σ_E, σ_N, E', and A_{dir} by the TK03 (BCE19) GGP models. (b) Black (σ_N) and light gray (σ_E, E', A_{dir}) dots correspond to 1,000 results from the bootstrap random resampling of the data distribution. Colored bars show resulting 95% confidence intervals.

Kiaman maintain the low standard deviations in the N-S direction (σ_N), overall variability (A_{dir}) smaller than predicted by the models, and the elongation of the distributions (E') close to 1 (see Figure 6b).

We applied two more stringent cutoff limits based on the number of sites ($N_S \geq 10$ and $N_S \geq 20$), and filtering procedures for within-site statistics, following the presented in Cromwell et al. (2018) and Tauxe and Kent (2004). Filtering of the data sets to $N_S \geq 10$ reduced the total number of directions by 15%, while the condition of $N_S \geq 20$ removed 48% (Figure 7a). The use of the filters based on intrasite statistics, $DC \geq 4$ with $n_e \geq 4$ and $k \geq 50$ and $n_e \geq 3$ and $k \geq 100$ (yellow and orange symbols, respectively, in Figure 7b) drastically reduced data size.

Results for bands that are now poorly populated have lost precision, as indicated by the wider confidence bars. Here again, the standard deviation in N-S direction (σ_N) is smaller than, and incompatible with, the
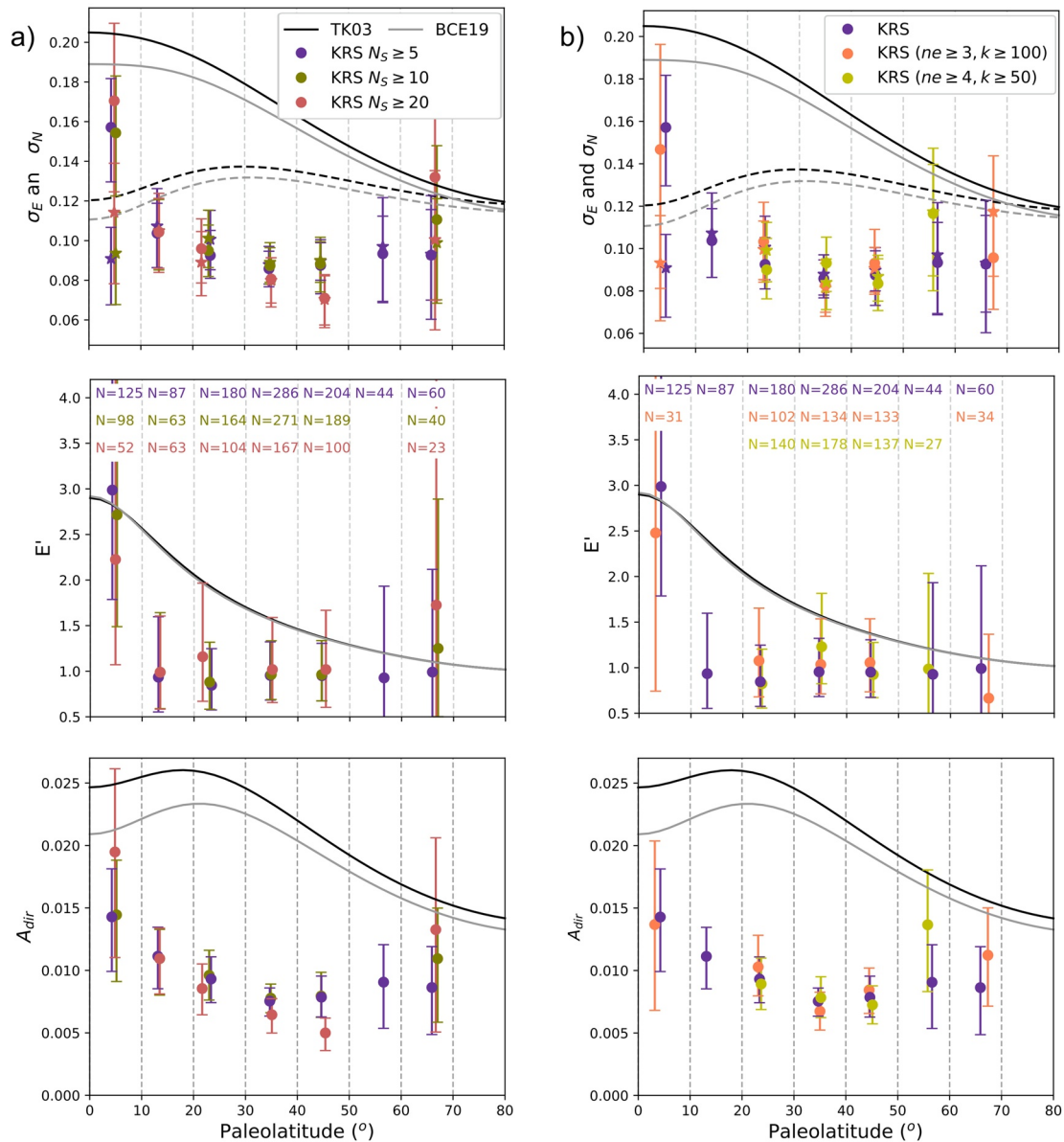
Figure 7. Directional paleosecular variation results using 10° of absolute paleolatitude (extrusive rocks only). Black and gray curves are the predictions from TK03 and BCE19 GGP models, of the standard deviation in x_E and x_N directions from equal-area projections of rotated distributions of directions ($\sigma_E \sigma_N$), elongation $E' = \sigma_{N^2}/\sigma_{E^2}$, and overall variability $A_{dir} = \sigma_E\sigma_N$). Stars are σ_E, and circles are σ_N. Left: other cutoff limits of the number of sites: $N_S \geq 10$ (dark blue) and $N_S \geq 20$ (olive green). Right: Other types of high-quality filtering data using the intrasite statistics $n_e \geq 3$ and $k \geq 100$ (orange); $DC \geq 4$, $n_e \geq 4$ and $k \geq 50$ (yellow). Results are listed in Table S2.

prediction of models TK03 and BCE19. The elongation is still nearly 1, and the overall variability diverges from the recent models for latitudes higher than 10°. Considering that a larger number of sites in any given study may imply a better determination of paleolatitudes and paleo-meridians, we might expect that filtering out sites with a low number of observations would result in better estimates for the N-S and E-W distributions. However, Figure 7 shows that the main characteristics of the PSV previously reported for the Kiaman database are preserved, with no overall improvement in fit to TK03 or BCE19. The use of the most restrictive filters produces wider confidence limits, due to the depleted number of data, but the results are essentially the same. Note that when applying the filter from Cromwell et al. (2018) all data from the 0°–20° bands are rejected. This prevents evaluating whether the more dispersed and elongated PSV distributions at equatorial latitudes can be confirmed for high-quality data.

Table 3
Summary of Parameters of Recent GGP Models and the Kiaman Minimum Models

Parameters of GGP models	TK03 Tauxe and Kent (2004) (0–5 Ma)	BCE19 Brandt et al. (2020) (0–10 Ma)	BB18 (cov) Bono et al. (2020) (0–10 Ma)	KRSM this study (320–260 Ma)	KRSCovM this study (320–260 Ma)
$\overline{g_1^0}\,(\mu T)$	−18	−18	−22.04	28.9	28.9
$\alpha\,(\mu T)$	7.5	6.7	12.25	8.8	10.6
β	3.8	4.2	2.82	3.8	3.1
$\sigma_1^0\,(\mu T)$	6.4	6.3	10.8	8.5	8.1
$RSD\,(g_1^0)$	35%	35%	49%	26%	25%
$\alpha\,/\,g_1^0$	42%	37%	55%	30%	37%
χ^2		63.5 (χ_{dir}^2)	105 ($\chi_{S_F}^2$)	95.3 (χ_{dir}^2)	62.7 (χ_{dir}^2)
$L = \sqrt{\chi^2\,/\,N}$		1.99 (L_{dir})	2.6 (L_{S_F})	2.61 (L_{dir})	2.11 (L_{dir})

Note. $RSD = \sigma_1^0\,/\,\left|g_1^0\right|$ is the relative standard deviation; χ_{dir}^2, L_{dir} misfit related to directional analyses N is the total number of estimates of σ_E and σ_N (two per band of latitude); $\chi_{S_F}^2, L_{S_F}$ misfits from Bono et al. (2020) N is the total number of estimates of S_F (one per band of latitude).

6. What was the Geomagnetic Field Like During the Kiaman Superchron?

The paleomagnetic directional database presented in this study is so far the most complete and largest list of site remanence directions for the Kiaman period. This list is available as PDKRS at the MagIC database (earthref.org/MagIC/16854). The database for the same time interval presented by Oliveira et al. (2018) is far more limited, comprising only nine igneous data sets due to the very restrictive filtering adopted. Our new Kiaman database, using more flexible criteria, resulted in a total of 1,459 reliable individual igneous directions from 91 data sets, of which 62 (1,017 directions) derived from extrusive rocks. After the application of a modified N-dependent A_{95} envelope, 1,385 directions (986 extrusives) remained.

The directional shape and scale analyses applied to the merged data sets using 10° paleolatitude bands present two distinctive behaviors: elongated and more disperse distributions near the Equator similar to the predictions of the TK03 and BCE19 models; and an essentially constant behavior of more concentrated and circular distributions for latitudes in the range 10°–70°. There are no systematic differences in the age that could explain the distinction between the Equatorial data and those from other latitudes. The only difference detected is that the quality of most of the Equatorial data cannot survive a more restrictive filtering process (empty and yellow bars at Figure 3b). It is not obvious how the lack of reliability of Equatorial data would contribute to greater elongation unless there is a systematic bias in the way sites are assigned to paleolatitude for that group. If GAD is an incorrect model for the TAF, and a quadrupolar mean is persistent in time, that could also contribute to lower inclination (most strongly near the equator), and could put sites in the wrong latitude. But probably it would not produce such a steep decrease of elongation. If this steep decrease in elongation is real then there could be a need to rethink GGP models (also true for high latitudes for the last million years, as discussed by Lawrence et al., 2009).

We searched for simplified (e.g., TK03 and BCE19) and covariant (using the same set of correlations as BB18) versions of GGP models for the extrusive members of the Kiaman database. The models (α and β, for a given $\overline{g_1^0}$) that minimize the square differences between the Kiaman data (σ_E, σ_N) are summarized in Table 3 (KRSM and KRSCovM). The model predictions are presented in Figure 8, where the purple and green curves indicate the simplified and covariant minimum models, respectively. The strength of $\overline{g_1^0}$ = 28.9 μT was set using the mean VDM of The World Paleointensity Database of Borok Geophysical Observatory (VDM = 7.47×10^{22} Am^2; from 177 paleointensity data of the interval 267–318 Ma).
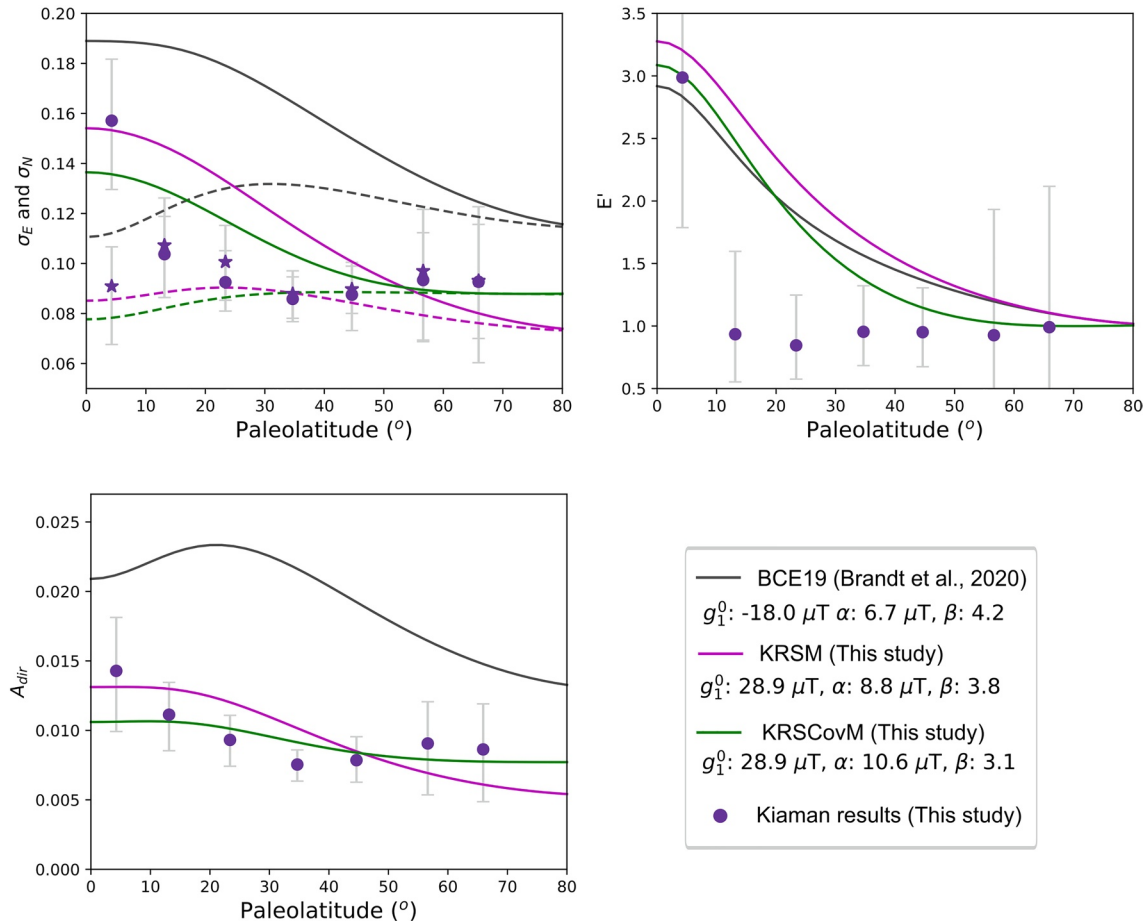
Figure 8. Directional PSV results using 10° bands of paleolatitude from only extrusive records of Kiaman (purple symbols), where σ_E, σ_N are the standard deviation in x_E and x_N equal-area coordinates from rotated distributions, $E' = \sigma_N^2 / \sigma_E^2$ is the elongation of distribution along the N-S direction, and $A_{dir} = \sigma_E \sigma_N$ is the overall variability of the distributions. Gray curves are the predicted values of σ_E, σ_N, E', and A_{dir} predicted by the BCE19 GGP model. Gray bars are the 95% confidence intervals given by bootstrap resampling. Green and purple curves are the best fit models fitted to the Kiaman results with and without the covariances between Gaussian coefficients proposed by Bono et al. (2020), respectively.

The differences between the Kiaman results and KRSCovM, KRSM, and BCE19 GGP models are, respectively, 0.7, 1.1, and 7.7 (average of normalized absolute deviation). This means that the Kiaman results are incompatible with the last 10 Myr field model BCE19.

The quality of the modeling can be accessed by the χ^2 misfit (Table 3) determined using the formulation presented by Bono et al. (2020), which considers the sum of quadratic differences between model and data, normalized by the variance of data. The normalized L^2 misfit is the ratio of χ^2 and the number of observations, the better the fit, the near to one is the normalized misfit. Table 3 includes the misfit using directional data (χ_{dir}^2), using the data of σ_E and σ_N, and their variances per latitude bin (models BCE19, KRSCovM, and KRSM), and the misfit from Bono's study (BB18 model misfit), which is based on the dispersion of VGPs data $\chi_{S_F}^2$. So, despite L_{dir} and L_{S_F} have similar sizes and are normalized, it is important to note that they are derived from different processes of modeling.

The insertion of the correlations between the Gaussian coefficients (Table 2 of Bono et al., 2020) improves the representation of the latitudinal dependence of Kiaman directional results by a GGP model. The covariant model has a lower difference between σ_N and σ_E at the Equator than the simplified model. The decay of this difference is condensed up to midlatitudes, as about 50° the dashed (σ_E) and continuous (σ_N) curves touch each other. This can be also observed at the elongation E' plot, where the elongation of the covariant model (green curve) reaches values comparable to 1 faster than for a simplified model (purple curve). Despite this, the covariant model still does not have the abrupt change in elongation seen in equatorial to

10° latitude bands for the data. The overall variability A_{dir} of Kiaman results is also better explained by the fitted covariant model (KRSCovM), the latitudinal dependence is smoother for the covariant model (green curve) and follows the latitudinal dependency of A_{dir} Kiaman results. In summary, the covariant version of GGP model (KRSCovM) is the best fitting model for Kiaman times, which has the lowest χ^2 misfit (Table 3). This result should be robust as the correlations used (Table 3 from Bono et al., 2020) were defined from dynamo simulations using reversing and non-reversing modes of the geomagnetic field. Therefore, this kind of behavior can be considered constant in Earth's geological past, or at least for these two studied periods.

The results found for the Kiaman β parameter, which multiplies the variances of antisymmetric families (Equation 3), giving a more significant predominance of dipole family variances, are similar to those found for the most recent few million years (see Table 3). The results for simplified GGP models KRSM (Kiaman) and BCE19 (0–10 Ma) are about four. For covariant versions, KRScovM (Kiaman) and BB18 (0–10 Ma) the β parameter are about three. This almost invariant in time β parameter was unexpected, as we had imagined that for a superchron, the ratio between antisymmetric and symmetric family contributions should be greater than that for times exhibiting field reversals as in the last few million years. However, this result is in agreement with recent findings of PSV modeling, Doubrovine et al. (2019) showed that the ratio of the shape parameters from Model G b/a found for the last 10 M.y. (Cromwell et al., 2018) is similar to the ratio for the superchron models (Doubrovine et al., 2019) and should not be considered as a proxy for reversal frequency. Therefore, our findings support a scenario where, like the ratio of b/a from Model G, the β parameter from GGP models seems to be the same for superchrons and the last few million years, indicating that, in terms of long-term variability of the geomagnetic field, the proportion between antisymmetric and symmetric families may be considered invariant.

Considering that the β parameter and the correlations from covariant models do not change throughout the geological time, the visible differences between the recent and Kiaman GGP models can be associated with the relative strength of the mean g_1^0 and the α parameter (Table 3). For a simplified or covariant model, the variances of the three orthogonal components of the geomagnetic field are linearly dependent on the α parameter, so this parameter affects the directional distribution, depending on the intensity of the mean field ($\overline{g_1^0}$). A confined directional distribution of unit vectors can be a result of the increase of the mean field (without changing the absolute variances of the field - α), or a diminishing of the variability of the field (α) without changing $\overline{g_1^0}$, or a composition of both. The models fitted for Kiaman Superchron have higher mean intensity (Table 3), as expected for a Superchron (see Kulakov et al., 2019), and although the absolute field variability is also higher than the last million years (see α in Table 3), it is not enough to maintain the same dispersion of the directional distribution (see the differences between models predictions of A_{dir}, Figure 8). So, the mean geomagnetic field for the Kiaman is stronger in intensity but less dispersed in its directional aspect.

For evaluating the relative variability of a GGP model we can use the ratio $\alpha/\overline{g_1^0}$, or the relative standard deviation of g_1^0 Gaussian coefficient (RSD, Table 3). The results are lower for the Kiaman Superchron than for the last million years (see Table 3) when comparing directly either simplified versions or the covariant versions of GGP models. One quantity that varies between the Kiaman superchron and the last 10 million years models is the ratio $\alpha/\overline{g_1^0}$, which can be found by modeling GGP using only directional data. For example, if we model a simplified GGP model for Kiaman results using the same intensity of BCE19 ($\overline{g_1^0} = 18\,\mu T$) we get $\beta = 3.8$ and $\alpha = 5.4$, which correspond to RSD of $\sigma_1^0/\overline{g_1^0} = 26\%$ and $\alpha/\overline{g_1^0} = 30\%$, the same relative variability as shown in Table 3. In other words, the previous knowledge of paleointensity is not necessary for finding the relative variability in simplified and covariant GGP modeling. Moreover, the mean strength used in this work should be considered with caution, as the mean VDM was calculated with the paleointesity data of Kiaman age, without any quality criteria commonly used for this type of data.

The persistent relation between symmetric and antisymmetric variances found for different periods (similar β results for 0−10 Ma, and Kiaman) indicates that during a reversing field mode the symmetric and antisymmetric families become more variable and in the same proportion. Therefore, what is really changing throughout the geological time is the mean intensity of the geomagnetic field (as observed for other periods, Kulakov et al., 2019) and the total relative variability of the field, that can be measured by $\alpha / \overline{g_1^0}$ or $\sigma_1^0/\overline{g_1^0}$

from directional GGP modeling. Using the comparison of the results from Kiaman (this work) with models from 0 to 10 Ma (Bono et al., 2020; Brandt et al., 2020), this relative variability is lower for epochs of Superchrons.

The comparison between Kiaman results and BCE19 model, which was fitted using the PSV10 database (Cromwell et al., 2018) is somewhat unrealistic, as the PSV10 database is more than twice the size of the Kiaman database in terms of the number of directions. Suppose we consider the same filtering of data for both databases, the size of the Kiaman database diminishes by half (Figure 3b). The inclusion of low-quality data is expected to increase overall variability. The effect of ill-determined mean directions increases the standard deviations σ_E and σ_N and produces more circular distributions (Brandt et al., 2020). Let us consider that the suppressed variation of the Kiaman results includes additional scattering sources related to possible underestimated experimental errors. It means that the actual Kiaman PSV was even lower than the results presented here, and the paleomagnetic field activity was even more subdued. Therefore, if the general behavior of the Kiaman geomagnetic field was like a GGP model, the small and circular determinations we have presented in this study can be explained by the result of underestimated experimental noise combined with a greatly reduced PSV of the geomagnetic field.

7. Final Remarks

The Kiaman igneous database (PDKRS, available in the MagIC Database) is the most complete list of paleomagnetic directions by site for the Kiaman period (267–318 Ma).

The Kiaman superchron is marked by low PSV, revealed by distributions of directions that are approximately circular, concentrated, and essentially invariant for latitudes higher than 10°. This behavior is entirely different from what is predicted by recent field GGP models.

We present the first GGP models fitted to ages older than the last 10 million years. Simplified and covariant GGP models that could be representative of this singular behavior arose from least squares fitting to σ_E and σ_N, following the procedure of Brandt et al. (2020). The best model found was the covariant-type KRScovM, which includes correlations between some pairs of Gaussian coefficients: $\left(g_1^0, g_3^0\right)$, $\left(g_1^1, g_3^1\right)\left(h_1^1, h_3^1\right)$, $\left(g_2^0, g_4^0\right)$, $\left(g_2^1, g_4^1\right)$, $\left(h_2^1, h_4^1\right)$, $\left(g_2^2, g_4^2\right)$, and $\left(h_2^2, h_4^2\right)$ (Table 3 of Bono et al., 2020). This result indicates that these correlations seem to be unchanged in the geological past for Earth's field, or at least for the two analyzed periods: the last 10 million (Bono et al., 2020) years and the Kiaman superchron (this study).

The resulting models have similar β parameter and $\alpha/\overline{g_1^0}$ lower than the last 10 million years. This indicates that during a non-reversing field, the variance of the field relative to $\overline{g_1^0}$ is suppressed. For a reversing mode, it is not only the symmetric families that become more variable, but also the antisymmetric in the same proportion. Therefore, if we want to access information about changes in the geomagnetic behavior across geological time, we should look to the paleointensity and/or the total relative variability, which in GGP modeling can be accessed by $\alpha/\overline{g_1^0}$. Recent findings using numerical dynamo modeling, Model G and paleointensity results from Cretaceous Superchron, Mid-Jurassic, and the last 10 Myr, point to the same line of thinking, where the shape parameter a from Model G and the median paleointensity are the most reliable parameters for determining changes in the field behavior (Sprain et al., 2020).

In the extreme case of very low PSV during the Kiaman, data uncertainty could dominate both the shape and scale in directional analyses and VGP scatter analyses. Therefore, it is recommended that in future work to study the long-term variations, more rigorous work must be adopted, producing higher k and a larger number of data per site to better estimate the uncertainty of the directional data.

Data Availability Statement

The complete list of paleomagnetic directions of PDKRS can be found at earthref.org/MagIC/16854 (http://dx.doi.org/10.7288/V4/MAGIC/16854).

References

Abrajevitch, A., Van der Voo, R., Bazhenov, M. L., Levashova, N. M., & McCausland, P. J. A. (2008). The role of the Kazakhstan orocline in the late Paleozoic amalgamation of Eurasia. *Tectonophysics*, *455*, 61–76. https://doi.org/10.1016/j.tecto.2008.05.006

Ali, J. R., Cheung, H. M. C., Aitchison, J. C., & Sun, Y. D. (2013). Paleomagnetic re-investigation of Early Permian rift basalts from the Baoshan Block, SW China: Constraints on the site-of-origin of the Gondwana-derived eastern Cimmerian terranes. *Geophysical Journal International*, *193*, 650–663. https://doi.org/10.1093/gji/ggt012

Amit, H., & Olson, P. (2015). Lower mantle superplume growth excites geomagnetic reversals. *Earth and Planetary Science Letters*, *414*, 68–76. https://doi.org/10.1016/j.epsl.2015.01.013

Aubele, K., Bachtadse, V., Muttoni, G., & Ronchi, A. (2014). Paleomagnetic data from late Paleozoic dikes of Sardinia: Evidence for block rotations and implications for the intra-Pangea megashear system. *Geochemistry, Geophysics, Geosystems*, *15*, 1684–1697. https://doi.org/10.1002/2014gc005325

Audibert, M., & Bazhenov, M. L. (1992). Permian paleomagnetism of the northern Tien-shan and its tectonic implications. *Tectonics*, *11*, 1057–1070. https://doi.org/10.1029/92tc01004

Bachtadse, V., Zanglein, R., Tait, J., & Soffel, H. C. (2002). Paleomagnetism of the Permo/Carboniferous (280 Ma) Jebel Nehoud ring complex, Kordofan, Central Sudan. *Journal of African Earth Sciences*, *35*, 89–97. https://doi.org/10.1016/s0899-5362(02)00006-4

Bazhenov, M. L., Van der Voo, R., Menzo, Z., Dominguez, A. R., Meert, J. G., & Levashova, N. M. (2016). Paleomagnetism and dating of a thick lava pile in the Permian Bakaly formation of eastern Kazakhstan: Regularities and singularities of the paleomagnetic record in thick lava series. *Physics of the Earth and Planetary Interiors*, *253*, 5–20. https://doi.org/10.1016/j.pepi.2016.02.001

Beck, M. E., Garcia, R. A., Burmester, R. F., Munizaga, F., Herve, F., & Drake, R. E. (1991). Paleomagnetism and geochronology of late Paleozoic Granitic-rocks from the lake district of southern Chile: Implications for accretionary tectonics. *Geology*, *19*, 332–335. https://doi.org/10.1130/0091-7613(1991)019<0332:pagolp>2.3.co;2

Belica, M. E., Tohver, E., Pisarevsky, S. A., Jourdan, F., Denyszyn, S., & George, A. D. (2017). Middle Permian paleomagnetism of the Sydney Basin, Eastern Gondwana: Testing Pangea models and the timing of the end of the Kiaman Reverse Superchron. *Tectonophysics*, *699*, 178–198. https://doi.org/10.1016/j.tecto.2016.12.029

Biggin, A. J., McCormack, A., & Roberts, A. (2010). Paleointensity database updated and upgraded. *Eos, Transactions American Geophysical Union*, *91*(2), 15. https://doi.org/10.1029/2010EO020003

Biggin, A. J., Strik, G., & Langereis, C. G. (2008). Evidence for a very-long-term trend in geomagnetic secular variation. *Nature Geoscience*, *1*, 395–398. https://doi.org/10.1038/ngeo181

Biggin, A. J., Van Hinsbergen, D. J. J., Langereis, C. G., Straathof, G. B., & Deenen, M. H. L. (2008). Geomagnetic secular variation in the Cretaceous Normal Superchron and in the Jurassic. *Physics of the Earth and Planetary Interiors*, *169*, 3–19. https://doi.org/10.1016/j.pepi.2008.07.004

Birkenmajer, K., Grocholski, A., Milewic, J. Z., & Nairn, A. E. M. (1968). *Paleomagnetic studies of Polish rocks: II. the upper Carboniferous and lower Permian of the Sudetes*. 435–474.

Birkenmajer, K., & Nairn, A. E. (1964). Paleomagnetic studies of Polish rocks: I. The Permian igneous rocks of the Kraków District and some results from the Holy Cross Mountains. In A. E. Nairn (Ed.), Annales Societatis Geologorum Poloniae (pp. 225–244).

Bolshakov, A. S., Solodovnikov, G. M., & Vinogradov, Y. K. (1989). Paleointensity of the geomagnetic field in the early Permian. *Izvestiya Akademii Nauk Sssr Fizika Zemli*, 70–78.

Bono, R. K., Biggin, A. J., Holme, R., Davies, C. J., Meduri, D. G., & Bestard, J. (2020). Covariant giant Gaussian process models with improved reproduction of paleosecular variation. *Geochemistry, Geophysics, Geosystems*, *21*, e2020GC008960. https://doi.org/10.1029/2020GC008960

Brandt, D., Constable, C., & Ernesto, M. (2020). Giant Gaussian process models of geomagnetic paleosecular variation: A directional outlook. *Geophysical Journal International*, *222*(3), 1526–1541. https://doi.org/10.1093/gji/ggaa258

Brandt, D., Ernesto, M., Constable, C., Franco, D. R., Carlos Weinschutz, L., de Oliveira Carvalho Rodrigues, P., et al. (2019). New late Pennsylvanian paleomagnetic results from Paraná Basin (Southern Brazil): Is the recent giant Gaussian process model valid for the Kiaman Superchron? *Journal of Geophysical Research: Solid Earth*, *124*, 6223–6242. https://doi.org/10.1029/2018jb016968

Brandt, D., Ernesto, M., Rocha-Campos, A. C., & dos Santos, P. R. (2009). Paleomagnetism of the Santa Fe Group, central Brazil: Implications for the late Paleozoic apparent polar wander path for South America. *Journal of Geophysical Research: Solid Earth*, *114*, 19. https://doi.org/10.1029/2008jb005735

Briden, J. C. (1966). Variation of intensity of the paleomagnetic field through geological time. *Nature*, *212*, 246–247. https://doi.org/10.1038/212246a0

Bylund, G. (1974). Paleomagnetism of dykes along the southern margin of the Baltic Shield. *Geologiska Föreningen i Stockholm Förhandlingar*, *96*(3), 231–235. https://doi.org/10.1080/11035897409454949

Clark, D. A., & Lackie, M. A. (2003). Paleomagnetism of the Early Permian Mount Leyshon intrusive complex and tuckers igneous complex, North Queensland, Australia. *Geophysical Journal International*, *153*, 523–547. https://doi.org/10.1046/j.1365-246x.2003.01907.x

Constable, C. G., & Johnson, C. L. (1999). Anisotropic paleosecular variation models: Implications for geomagnetic field observables. *Physics of the Earth and Planetary Interiors*, *115*, 35–51. https://doi.org/10.1016/s0031-9201(99)00065-5

Constable, C. G., & Parker, R. L. (1988). Statistics of the geomagnetic secular variation for the past 5 m.y. *Journal of Geophysical Research: Solid Earth and Planets*, *93*, 11569–11581. https://doi.org/10.1029/jb093ib10p11569

Cornwell, J. D. (1967). Paleomagnetism of Exeter Lavas Devonshire. *Geophysical Journal of the Royal Astronomical Society*, *12*, 181–196. https://doi.org/10.1111/j.1365-246x.1967.tb03114.x

Cottrell, R. D., Tarduno, J. A., & Roberts, J. (2008). The Kiaman Reversed Polarity Superchron at Kiama: Toward a field strength estimate based on single silicate crystals. *Physics of the Earth and Planetary Interiors*, *169*, 49–58. https://doi.org/10.1016/j.pepi.2008.07.041

Cromwell, G., Johnson, C., Tauxe, L., Constable, C., & Jarboe, N. (2018). PSV10: A Global Data Set for 0–10 Ma Time-averaged field and paleosecular variation studies. *Geochemistry, Geophysics, Geosystems*.

De Boer, J., & Brookins, D. G. (1972). Paleomagnetic and radiometric age determination of (Permian) pegmatites in Middletown district (connecticut). *Earth and Planetary Science Letters*, *15*, 140–144. https://doi.org/10.1016/0012-821x(72)90054-4

Deenen, M. H. L., Langereis, C. G., van Hinsbergen, D. J. J., & Biggin, A. J. (2011). Geomagnetic secular variation and the statistics of paleomagnetic directions. *Geophysical Journal International*, *186*, 509–520. https://doi.org/10.1111/j.1365-246x.2011.05050.x

de Oliveira, W. P., Franco, D. R., Brandt, D., Ernesto, M., Neto, C. F. D., Zhao, X. X., et al. (2018). Behavior of the paleosecular variation during the Permian-Carboniferous reversed Superchron and comparisons to the low reversal frequency intervals since Precambrian times. *Geochemistry, Geophysics, Geosystems*, *19*, 1035–1048. https://doi.org/10.1002/2017gc007262

Dietzel, G. F. L. (1960). *Geology and Permian paleomagnetism of the Merano region, province of Bolzano, N. Italy*. PhD thesis. Utrecht University.

Domeier, M., Van der Voo, R., & Denny, F. B. (2011a). Widespread inclination shallowing in Permian and Triassic paleomagnetic data from Laurentia: Support from new paleomagnetic data from Middle Permian shallow intrusions in southern Illinois (USA) and virtual geomagnetic pole distributions. *Tectonophysics*, *511*, 38–52. https://doi.org/10.1016/j.tecto.2011.08.016

Domeier, M., Van der Voo, R., Tohver, E., Tomezzoli, R. N., Vizan, H., Torsvik, T. H., & Kirshner, J. (2011b). New Late Permian paleomagnetic data from Argentina: Refinement of the apparent polar wander path of Gondwana. *Geochemistry, Geophysics, Geosystems*, *12*. https://doi.org/10.1029/2011gc003616

Domeier, M., Van der Voo, R., Tomezzoli, R. N., Tohver, E., Hendriks, B. W. H., Torsvik, T. H., et al. (2011c). Support for an "A-type" Pangea reconstruction from high-fidelity Late Permian and Early to Middle Triassic paleomagnetic data from Argentina. *Journal of Geophysical Research: Solid Earth*, *116*. https://doi.org/10.1029/2011jb008495

Dominguez, A. R., Van der Voo, R., Torsvik, T. H., Hendriks, B. W. H., Abrajevitch, A., Domeier, M., et al. (2011). The similar to 270 Ma paleolatitude of Baltica and its significance for Pangea models. *Geophysical Journal International*, *186*, 529–550. https://doi.org/10.1111/j.1365-246x.2011.05061.x

Dooley, R. E. (1983). Paleomagnetism of some mafic intrusions in the South-Carolina Piedmont.1. Magnetic systems with single characteristic directions. *Physics of the Earth and Planetary Interiors*, *31*, 241–268. https://doi.org/10.1016/0031-9201(83)90101-2

Doubrovine, P. V., Veikkolainen, T., Pesonen, L. J., Piispa, E., Ots, S., Smirnov, A. V., et al. (2019). Latitude dependence of geomagnetic paleosecular variation and its relation to the frequency of magnetic reversals: Observations from the Cretaceous and Jurassic. *Geochemistry, Geophysics, Geosystems*, *20*, 1240–1279. https://doi.org/10.1029/2018gc007863

Driscoll, P. E., & Evans, D. A. D. (2016). Frequency of Proterozoic geomagnetic superchrons. *Earth and Planetary Science Letters*, *437*, 9–14. https://doi.org/10.1016/j.epsl.2015.12.035

Edel, J. B., Montigny, R., & Thuizat, R. (1981). Late Paleozoic rotations of Corsica and Sardinia: New evidence from paleomagnetic and K-Ar studies. *Tectonophysics*, *79*, 201–223. https://doi.org/10.1016/0040-1951(81)90113-x

Esang, C. B., & Piper, J. D. A. (1984). Paleomagnetism of the Carboniferous E-W dyke swarm in Argyllshire. *Scottish Journal of Geology*, *20*, 309–314. https://doi.org/10.1144/sjg20030309

Fisher, R. (1953). Dispersion on a sphere. *Proceedings of the Royal Society of London A: Mathematical and Physical Sciences*, *217*, 295–305. https://doi.org/10.1098/rspa.1953.0064

Franco, D. R., Ernesto, M., Ponte-Neto, C. F., Hinnov, L. A., Berquo, T. S., Fabris, J. D., & Rosiere, C. A. (2012). Magnetostratigraphy and mid-paleolatitude VGP dispersion during the Permo-Carboniferous Superchron: Results from Parana Basin (Southern Brazil) rhythmites. *Geophysical Journal International*, *191*, 993–1014.

Gallo, L. C., Tomezzoli, R. N., & Cristallini, E. O. (2017). A pure dipole analysis of the Gondwana apparent polar wander path: Paleogeographic implications in the evolution of Pangea. *Geochemistry, Geophysics, Geosystems*, *18*, 1499–1519. https://doi.org/10.1002/2016gc006692

Garcia, A., Thomas, N., Liss, D., & Shaw, J. (2006). Low geomagnetic field intensity during the Kiaman superchron: Thellier and microwave results from the Great Whin Sill intrusive complex, northern United Kingdom. *Geophysical Research Letters*, *33*. https://doi.org/10.1029/2006GL026729

Geuna, S. E., & Escosteguy, L. D. (2004). Paleomagnetism of the upper Carboniferous-lower Permian transition from Paganzo Basin, Argentina. *Geophysical Journal International*, *157*, 1071–1089. https://doi.org/10.1111/j.1365-246x.2004.02229.x

Haldan, M. M., Langereis, C. G., Biggin, A. J., Dekkers, M. J., & Evans, M. E. (2009). A comparison of detailed equatorial red bed records of secular variation during the Permo-Carboniferous Reversed Superchron. *Geophysical Journal International*, *177*, 834–848. https://doi.org/10.1111/j.1365-246x.2009.04124.x

Haldan, M. M., Meijers, M. J. M., Langereis, C. G., Larsen, B. T., & Heyer, H. (2014). New paleomagnetic results from the Oslo Graben, a Permian Superchron lava province. *Geophysical Journal International*, *199*, 1554–1571. https://doi.org/10.1093/gji/ggu351

Halvorsen, E. (1970). Paleomagnetism and the age of the younger diabases in the Ny-Hellesund area, S. Norway. *Norsk Geologisk Tidsskrift*, 157–166.

Harcombe-Smee, B. J., Piper, J. D. A., Rolph, T. C., & Thomas, D. N. (1996). A paleomagnetic and paleointensity study of the Mauchline lavas, south-west Scotland. *Physics of the Earth and Planetary Interiors*, *94*, 63–73. https://doi.org/10.1016/0031-9201(95)03083-2

Haston, R. B., Luyendyk, B. P., Landis, C. A., & Coombs, D. S. (1989). Paleomagnetism and question of original location of the Permian brook-street terrane, new-zealand. *Tectonics*, *8*, 791–801. https://doi.org/10.1029/tc008i004p00791

Heiniger, C. (1979). Paleomagnetic and rockmagnetic properties of the Permian volcanics in the western southern Alps. *Journal of Geophysics-Zeitschrift Fur Geophysik*, *46*, 397–411.

Hounslow, M. W. (2016). Geomagnetic reversal rates following Palaeozoic superchrons have a fast restart mechanism. *Nature Communications*, *7*. https://doi.org/10.1038/ncomms12507

Hounslow, M. W., & Balabarov, Y. P. (2016). A geomagnetic polarity timescale for the Permian, calibrated to stage boundaries. *Geological Society, London, Special Publications*, *450*, 61–103. https://doi.org/10.1144/sp450.8

Huang, K. N., & Opdyke, N. D. (1991). Paleomagnetic results from the upper Carboniferous of the Shan-Thai-Malay block of western yunnan, China. *Tectonophysics*, *192*, 333–344. https://doi.org/10.1016/0040-1951(91)90107-4

Irving, E. (1977). Drift of major continental blocks since Devonian. *Nature*, *270*, 304–309. https://doi.org/10.1038/270304a0

Jesinkey, C., Forsythe, R. D., Mpodozis, C., & Davidson, J. (1987). Concordant late Paleozoic paleomagnetizations from the Atacama Desert: Implications for tectonic models of the Chilean Andes. *Earth and Planetary Science Letters*, *85*, 461–472. https://doi.org/10.1016/0012-821x(87)90141-5

Klootwijk, C. T. (2002). Carboniferous paleomagnetism of the Rocky Creek Block, northern Tamworth Belt, and the New England pole path. *Australian Journal of Earth Sciences*, *49*, 375–405. https://doi.org/10.1046/j.1440-0952.2002.00924.x

Klootwijk, C. T. (2003). Carboniferous paleomagnetism of the Werrie Block, northwestern Tamworth Belt, and the New England pole path. *Australian Journal of Earth Sciences*, *50*, 865–902. https://doi.org/10.1111/j.1400-0952.2003.01032.x

Konrad, H. J., & Nairn, A. E. M. (1972). Paleomagnetism of Permian rocks of black forest, Germany. *Geophysical Journal of the Royal Astronomical Society*, *27*, 369–382. https://doi.org/10.1111/j.1365-246x.1972.tb06098.x

Krs, M. (1967). Intensity of the Earth's magnetic field in the geological past. *Nature*, *215*, 697–699. https://doi.org/10.1038/215697a0

Kulakov, E. V., Sprain, C. J., Doubrovine, P. V., Smirnov, A. V., Paterson, G. A., Hawkins, L., et al. (2019). Analysis of an updated paleointensity database (QPI-PINT) for 65–200 Ma: Implications for the long-term history of dipole moment through the Mesozoic. *Journal of Geophysical Research: Solid Earth*, *124*, 9999–10022. https://doi.org/10.1029/2018JB017287

Lackie, M. A., French, D. H., & Clark, D. A. (1992). Magnetic mineralogy of felsic volcanics of the conway-bimurra area, northeast queensland: relationships to aeromagnetic anomalies and hydrothermal alteration.

Lackie, M. A., & Schmidt, P. W. (1993). Remagnetization of strata during the hunter-bowen orogeny. *Exploration Geophysics*, *24*, 269–274. https://doi.org/10.1071/eg993269

Larson, R. L., & Olson, P. (1991). Mantle plumes control magnetic reversal frequency. *Earth and Planetary Science Letters*, *107*(3–4), 437–447. https://doi.org/10.1016/0012-821X(91)90091-U

Lawrence, K. P., Tauxe, L., Staudigel, H., Constable, C. G., Koppers, A., McIntosh, W., & Johnson, C. L. (2009). Paleomagnetic field properties at high southern latitude. *Geochemistry, Geophysics, Geosystems*, *10*. https://doi.org/10.1029/2008gc002072

Levashova, N. M., Degtyarev, K. E., Bazhenov, M. L., Collins, A. Q., & Van der Voo, R. (2003). Permian paleomagnetism of East Kazakhstan and the amalgamation of Eurasia. *Geophysical Journal International*, *152*, 677–687. https://doi.org/10.1046/j.1365-246x.2003.01879.x

Li, Y. P., Sharps, R., McWilliams, M., Li, Y. G., Li, Q., & Zhang, W. (1991). Late Paleozoic paleomagnetic results from the Junggar block, northwestern China. *Journal of Geophysical Research: Solid Earth*, *96*, 16047–16060. https://doi.org/10.1029/91jb01619

Li, Y. P., Sharps, R., McWilliams, M., Nur, A., Li, Y. G., Li, Q., & Zhang, W. (1989). Paleomagnetic results from late Paleozoic dikes from the northwestern Junggar block, northwestern china. *Earth and Planetary Science Letters*, *94*, 123–130. https://doi.org/10.1016/0012-821x(89)90088-5

Liss, D., Owens, W. H., & Hutton, D. H. W. (2004). New paleomagnetic results from the Whin Sill complex: Evidence for a multiple intrusion event and revised virtual geomagnetic poles for the late Carboniferous for the British Isles. *Journal of the Geological Society*, *161*, 927–938. https://doi.org/10.1144/0016-764903-156

Mauritsch, H. J., & Rother, K. (1983). Paleomagnetic investigations in the Thuringer forest (GDR). *Tectonophysics*, *99*, 63–72. https://doi.org/10.1016/0040-1951(83)90170-1

McElhinny, M. W., & Lock, J. (1996). IAGA paleomagnetic databases with access. *Surveys in Geophysics*, *17*, 575–591. https://doi.org/10.1007/bf01888979

McElhinny, M. W., & McFadden, P. L. (1997). Paleosecular variation over the past 5 Myr based on a new generalized database. *Geophysical Journal International*, *131*, 240–252. https://doi.org/10.1111/j.1365-246x.1997.tb01219.x

McFadden, P. L., Merrill, R. T., & McElhinny, M. W. (1988). Dipole quadrupole family modeling of paleosecular variation. *Journal of Geophysical Research: Solid Earth and Planets*, *93*, 11583–11588. https://doi.org/10.1029/jb093ib10p11583

McFadden, P. L., Merrill, R. T., McElhinny, M. W., & Lee, S. H. (1991). Reversals of the Earth's magnetic field and temporal variations of the dynamo families. *Journal of Geophysical Research: Solid Earth and Planets*, *96*, 3923–3933. https://doi.org/10.1029/90jb02275

Menzo, Z. (2013). Permian secular variation of the Ayaguz formation in Kazakhstan.

Muttoni, G., Kent, D. V., Garzanti, E., Brack, P., Abrahamsen, N., & Gaetani, M. (2003). Early Permian Pangea 'B' to Late Permian Pangea 'A'. *Earth and Planetary Science Letters*, *215*, 379–394. https://doi.org/10.1016/s0012-821x(03)00452-7

Ogg, J. G. (2012a). Geomagnetic polarity time scale. In F. M. Gradstein, J. G. Ogg, M. G. Schmitz, & G. M. Ogg (Eds.), The geologic time scale (pp. 85–113). Boston, MA: Elsevier. https://doi.org/10.1016/B978-0-444-59425-9.00005-6

Ogg, J. G. (2012b). Geomagnetic polarity time scale. In F. M. Gradstein, J. G. Ogg, M. G. Schmitz, & G. M. Ogg (Eds.), The geologic time scale (pp. 85–113). Boston, MA: Elsevier. https://doi.org/10.1016/B978-0-444-59425-9.00005-6

Opdyke, N. D., & Channell, J. (1996). Magnetic Stratigraphy, International geophysics series (Vol. 64, pp. 1–8). San Diego: Academic Press. https://doi.org/10.1016/s0074-6142(06)80003-3 Introduction and History online resource (xiv, 346 pages).

Opdyke, N. D., Roberts, J., Claoue-Long, J., Irving, E., & Jones, P. J. (2000). Base of the Kiaman: Its definition and global stratigraphic significance. *Geological Society of America Bulletin*, *112*, 1315–1341. https://doi.org/10.1130/0016-7606(2000)112<1315:botkid>2.0.co;2

Pavlov, V. E., Veselovskiy, R. V., Shatsillo, A. V., & Gallet, Y. (2012). Magnetostratigraphy of the Ordovician Angara/Rozhkova River section: Further evidence for the Moyero reversed superchron. *Izvestiya - Physics of the Solid Earth*, *48*, 297–305. https://doi.org/10.1134/s1069351312040052

Piper, J. D. A. (1992). Paleomagnetic properties of a Precambrian metamorphic terrane: The Lewisian complex of the Outer Hebrides, NW Scotland. *Tectonophysics*, *201*, 17–48. https://doi.org/10.1016/0040-1951(92)90173-4

Pisarevsky, S. A., Gladkochub, D. P., Donskaya, T. A., De Waele, B., & Mazukabzov, A. M. (2006). Paleomagnetism and geochronology of mafic dykes in south Siberia, Russia: The first precisely dated Early Permian paleomagnetic pole from the Siberian craton. *Geophysical Journal International*, *167*, 649–658. https://doi.org/10.1111/j.1365-246x.2006.03160.x

Quidelleur, X., & Courtillot, V. (1996). On low-degree spherical harmonic models of paleosecular variation. *Physics of the Earth and Planetary Interiors*, *95*, 55–77. https://doi.org/10.1016/0031-9201(95)03115-4

Rapalini, A. E., & Vilas, J. F. (1991). Tectonic rotations in the late Paleozoic continental-margin of southern South-America determined and dated by paleomagnetism. *Geophysical Journal International*, *107*, 333–351.

Rapalini, A. E., Vilas, J. F., Bobbio, M. L., & Valencio, D. A. (1989). Goedynamic interpretations from paleomagnetic data of late Paleozoic rocks in the southern Andes. *Deep Structure and past Kinematics of Accreted Terranes* (pp. 41–57).

Schwarz, E. J., & Symons, D. T. A. (1969). Geomagnetic intensity between 100 million and 2500 million years ago. *Physics of the Earth and Planetary Interiors*, *2*, 11–18. https://doi.org/10.1016/0031-9201(69)90014-4

Senanayake, W. E., & McElhinny, M. W. (1983). A paleointensity method for use with highly oxidized basalts, and application to some Permian volcanics. *Journal of Geophysics*, *52*, 85–96.

Shaanan, U., Rosenbaum, G., Pisarevsky, S., & Speranza, F. (2015). Paleomagnetic data from the New England Orogen (eastern Australia) and implications for oroclinal bending. *Tectonophysics*, *664*, 182–190. https://doi.org/10.1016/j.tecto.2015.09.018

Sharps, R., McWilliams, M., Li, Y., Cox, A., Zhang, Z., Zhai, Y., et al. (1989). Lower Permian paleomagnetism of the Tarim block, northwestern China. *Earth and Planetary Science Letters*, *92*, 275–291. https://doi.org/10.1016/0012-821x(89)90052-6

Shatsillo, A. V., Fedyukin, I. V., & Powerman, V. I. (2014). Paleomagnetism of the Late Paleozoic granites of the Angara-Vitim batholith and the host rocks of the Baikal-Patom folded area: Tectonic implications. *Russian Geology and Geophysics*, *55*, 864–880. https://doi.org/10.1016/j.rgg.2014.06.006

Shcherbakov, V. P., & Sycheva, N. K. (2013). On the intensity of the geomagnetic field in the geological past. *Izvestiya, Physics of the Solid Earth*, *49*, 699–717. https://doi.org/10.1134/S1069351313040095

Shcherbakova, V. V., Shcherbakov, V. P., Vodovosov, V. V., & Sycheva, N. K. (2005). Paleointensity at the PermianTriassic Boundaryand in the Late Permian. *Izvestiya, Physics of the Solid Earth*, *41*, 931–944.

Smirnov, A. V., Tarduno, J. A., & Evans, D. A. D. (2011). Evolving core conditions ca. 2 billion years ago detected by paleosecular variation. *Physics of the Earth and Planetary Interiors*, *187*, 225–231. https://doi.org/10.1016/j.pepi.2011.05.003

Soffel, H. C., & Harzer, F. (1991). An upper Carboniferous-lower Permian (280 ma) paleomagnetic pole from the western margin of the Bohemian Massif. *Geophysical Journal International*, *105*, 547–551. https://doi.org/10.1111/j.1365-246x.1991.tb06733.x

Solodovnikov, G. M. (1992a). Paleointensity of the geomagnetic field in the Lower Permian. *Izv. Acad. Sci., Phys. Solid Earth*, 718–722.

Solodovnikov, G. M. (1992b). Paleostrength of geomagnetic field in Middle-Late Carboniferous. *Izvestiya, Physics of the Solid Earth.*, 327–331.

Song, P., Ding, L., Li, Z., Lippert, P. C., & Yue, Y. (2017). An early bird from Gondwana: Paleomagnetism of Lower Permian lavas from northern Qiangtang (Tibet) and the geography of the Paleo-Tethys. *Earth and Planetary Science Letters*, *475*, 119–133. https://doi.org/10.1016/j.epsl.2017.07.023

Sprain, C. J., Biggin, A., Bono, R., Davies, C. J., Paterson, G. A., Hawkins, L., et al. (2020). Assessing the Robustness of Long-term Field Variations in the Paleomagnetic Record. AGU Fall Meeting, GP008-0004.

Stojanovic, D., Aitchison, J. C., Ali, J. R., Ahmad, T., & Dar, R. A. (2016). Paleomagnetic investigation of the Early Permian Panjal Traps of NW India; regional tectonic implications. *Journal of Asian Earth Sciences*, *115*, 114–123. https://doi.org/10.1016/j.jseaes.2015.09.028

Tarduno, J. A., Cottrell, R. D., & Smirnov, A. V. (2006). The paleomagnetism of single silicate crystals: Recording geomagnetic field strength during mixed polarity intervals, superchrons, and inner core growth. *Reviews of Geophysics*, *44*. https://doi.org/10.1029/2005rg000189

Tauxe, L., & Kent, D. V. (2004). A simplified statistical model for the geomagnetic field and the detection of shallow bias in paleomagnetic inclinations: Was the ancient magnetic field dipolar? *Timescales of the Paleomagnetic Field*, *145*, 101–115.

Tauxe, L., & Kodama, K. P. (2009). Paleosecular variation models for ancient times: Clues from Keweenawan lava flows. *Physics of the Earth and Planetary Interiors*, *177*, 31–45. https://doi.org/10.1016/j.pepi.2009.07.006

Tauxe, L., Kodama, K. P., & Kent, D. V. (2008). Testing corrections for paleomagnetic inclination error in sedimentary rocks: A comparative approach. *Physics of the Earth and Planetary Interiors*, *169*, 152–165. https://doi.org/10.1016/j.pepi.2008.05.006

Tauxe, L., Shaar, R., Jonestrask, L., Swanson-Hysell, N. L., Minnett, R., Koppers, A. A. P., et al. (2016). PmagPy: Software package for paleomagnetic data analysis and a bridge to the Magnetics Information Consortium (MagIC) Database. *Geochemistry, Geophysics, Geosystems*, *17*, 2450–2463. https://doi.org/10.1002/2016gc006307

Thomas, D. N., Rolph, T. C., & Friel, D. F. (1997). Permo-Carboniferous (Kiaman) paleointensity results from the western Bohemian Massif, Germany. *Geophysical Journal International*, *130*, 257–265. https://doi.org/10.1111/j.1365-246x.1997.tb01004.x

Thomas, D. N., Rolph, T. C., & Shaw, J. (1995). Paleointensity results from the Permo-Carboniferous (Kiaman) reversed superchron : The Great Whin and Midland Valley sills of the northern United Kingdom. *Geophysical Journal International*, *123*, 798–816. https://doi.org/10.1111/j.1365-246x.1995.tb06891.x

Thompson, J. F. C., Guillaume, A., & Daly, L. (1986). Paleomagnetism of the Permian Volcanic rocks of Moissey (French Jura): Implications for the Palaeofield and Tectonic evolution. *Geophysical Journal International*, *86*, 103–117. https://doi.org/10.1111/j.1365-246x.1986.tb01075.x

Thorning, L., & Abrahamsen, N. (1980). Paleomagnetism of Permian multiple intrusion dykes in Bohuslän, SW Sweden. *Geophysical Journal International*, *60*, 163–185. https://doi.org/10.1111/j.1365-246x.1980.tb04288.x

Tomezzoli, R. N., Tickyj, H., Rapalini, A. E., Gallo, L. C., Cristallini, E. O., Arzadún, G., & Chemale, F. (2018). Gondwana's apparent polar wander path during the Permian-new insights from South America . *Sci Rep*, *8*, 8436. https://doi.org/10.1038/s41598-018-25873-z

Torsvik, T. H., Van der Voo, R., Preeden, U., Mac Niocaill, C., Steinberger, B., Doubrovine, P. V., et al. (2012). Phanerozoic polar wander, paleogeography and dynamics. *Earth-Science Reviews*, *114*, 325–368. https://doi.org/10.1016/j.earscirev.2012.06.007

Usui, Y., & Tian, W. (2017). Paleomagnetic directional groups and paleointensity from the flood basalt in the Tarim large igneous province: Implications for eruption frequency. *Earth Planets and Space*, *69*. https://doi.org/10.1186/s40623-016-0595-x

Van Dongen, P. G. (1967). The rotation of Spain: Paleomagnetic evidence from the eastern Pyrenees. *Palaeogeography, Palaeoclimatology, Palaeoecology*, *3*, 417–432. https://doi.org/10.1016/0031-0182(67)90028-4

Vandamme, D. (1994). A new method to determine paleosecular variation. *Physics of the Earth and Planetary Interiors*, *85*, 131–142. https://doi.org/10.1016/0031-9201(94)90012-4

Vigliotti, L., Alvarez, W., & McWilliams, M. (1990). No relative rotation detected between corsica and sardinia. *Earth and Planetary Science Letters*, *98*, 313–318. https://doi.org/10.1016/0012-821x(90)90033-t

Westphal, M., Orsini, J., & Vellutini, P. (1976). Le microcontinent corso-sarde, sa position initiale: Donnees paleomagnetiques et raccords geologiques. *Tectonophysics*, *30*, 141–157. https://doi.org/10.1016/0040-1951(76)90142-6

Wynne, P. J., Irving, E., & Osadetz, K. (1983). Paleomagnetism of the Esayoo formation (Permian) of northern Ellesmere island - Possible clue to the solution of the Nares strait dilemma. *Tectonophysics*, *100*, 241–256. https://doi.org/10.1016/0040-1951(83)90190-7

Xu, Y., Yang, Z., Tong, Y.-B., Wang, H., Gao, L., & An, C. (2015). Further paleomagnetic results for lower Permian basalts of the Baoshan Terrane, southwestern China, and paleogeographic implications. *Journal of Asian Earth Sciences*, *104*, 99–114. https://doi.org/10.1016/j.jseaes.2014.10.029

Yi, Z., Huang, B., Xiao, W., Yang, L., & Qiao, Q. (2015). Paleomagnetic study of Late Paleozoic rocks in the Tacheng Basin of West Junggar (NW China): Implications for the tectonic evolution of the western Altaids. *Gondwana Research*, *27*, 862–877. https://doi.org/10.1016/j.gr.2013.11.006

Yuan, K., Van der Voo, R., Bazhenov, M. L., Bakhmutov, V., Alekhin, V., & Hendriks, B. W. H. (2011). Permian and Triassic palaeolatitudes of the Ukrainian shield with implications for Pangea reconstructions. *Geophysical Journal International*, *184*, 595–610. https://doi.org/10.1111/j.1365-246x.2010.04889.x

Zijderveld, J. D., Dejong, K. A., & Vandervo, R. (1970). Rotation of Sardinia: Paleomagnetic evidence from Permian rocks. *Nature*, *226*, 933–934. https://doi.org/10.1038/226933a0

Zijderveld, J. D. A. (1967). The natural remanent magnetizations of the Exeter volcanic traps (Permian, Europe). *Tectonophysics*, *4*(2), 121–153. https://doi.org/10.1016/0040-1951(67)90048-0

Zijderveld, J. D. A., & De Jong, K. A. (1969). Paleomagnetism of some Late Paleozoic and Triassic rocks from the Eastern Lombardic Alps, Italy . *Geologie en Mijnbouw*, 559–564.